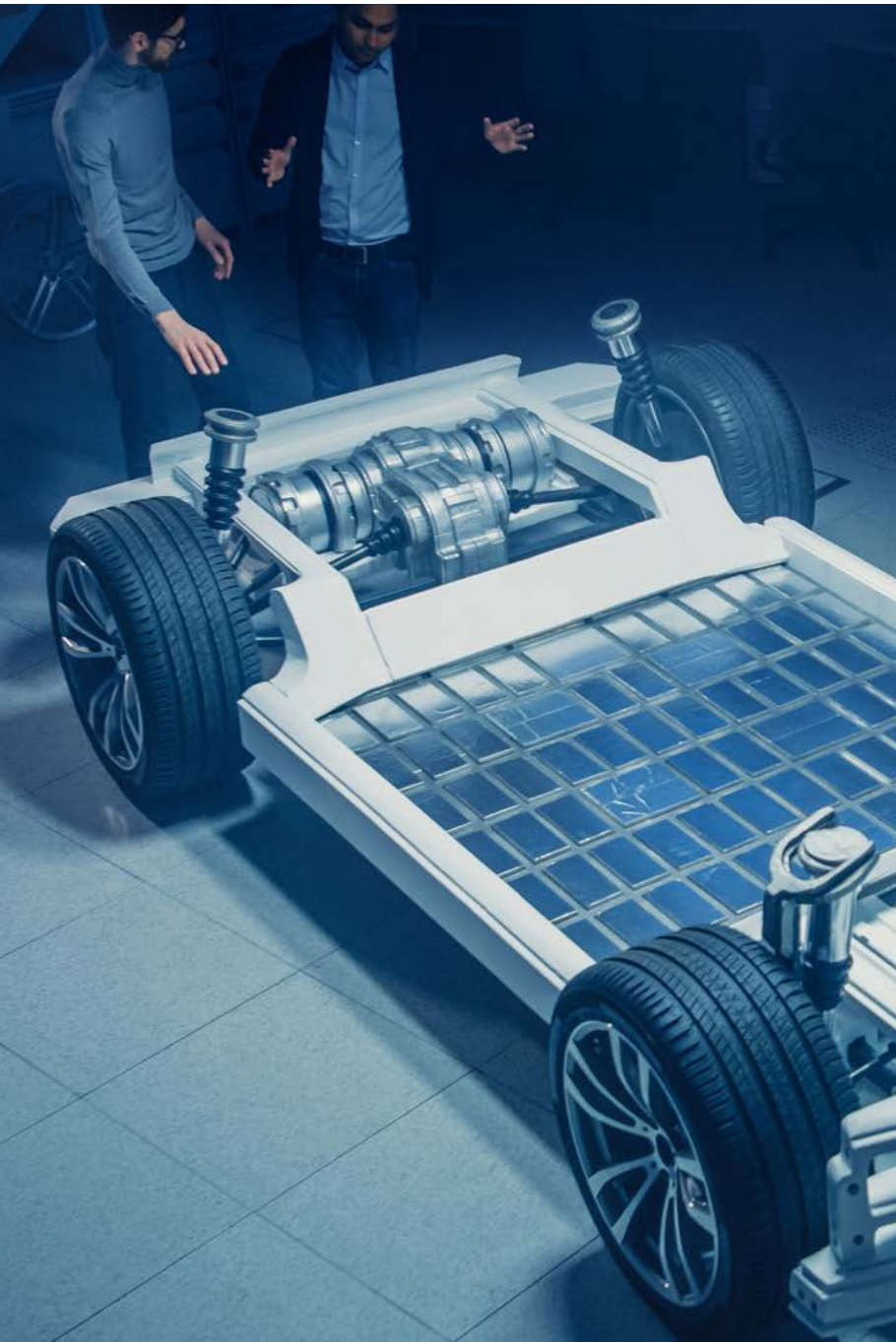electronics-cooling.com

electronics COOLING

2022 ANNUAL GUIDE

FEATURED TOPICS

TRANSPORTATION

ELECTRIC MOTORS

TWO-PHASE COOLING

MACHINE LEARNING

HEAT SINKS

THERMAL COMFORT

COOLING EVENTS

STATISTICAL ANALYSIS

PRODUCTS & SERVICES DIRECTORY

SPECIAL SECTION: SEMI-THERM 2022

ALPHA | Your partner for thermal solutions

Online Heatsink Customization

🏠 > Online Heatsink Customization

1: Specify Customization   2: Review Customization   3: Input Contact Information   4: Submit Request

Customization Summary [Units:mm]

Change Height / Thickness	Fin Height	17	Base Thickness	5
Add TIM	Type	T-PCM585-30S	Size	30 x 30
Add Pedestal	Size	30 sq.	Height	1.5

New Features

✔ 3D view is updated immediately, providing instant design visualization

✔ Improved customization user interface

✔ Fin removal can be specified

✔ 2D/3D drawings and quotes are available in 0-2 business days

✔ Proto lead time is 1-2 weeks with No tooling/NRE fees

www.alphanovatech.com

CONTENTS

LECTRIX®

EDITORIAL

Victor Chiriac
Co-Editor of ECM

Dear EC Readers,

As we start the New Year, I am honored to wish you all a Happy, Healthy and Prosperous New Year 2022! We count on each of you to make 2022 a great year, full of life and technology accomplishments!

The *Electronics Cooling* 2022 Annual Guide brings to you exciting articles, including Machine Learning for Phase Change materials, advanced cooling solutions for Electric Vehicles and Green Transportation, enhanced manifold heat sink devices, advanced methodologies for wireless and mobile applications and many more. We hope you will enjoy the first edition of EC in 2022 and will contribute to our future issues!

Looking back at 2021, we all hoped to leave behind the Covid-19 pandemic, yet 2022 still finds us dealing with it at a global level. Although there are many challenges to overcome, there is also a lot of hope, growth and opportunity ahead. New technologies are being adopted as a result of the shift in the workforce, health and social behaviors. According to various industry experts at the CES event in Las Vegas a few weeks ago, the technology demand in 2021 was strong with 15-40% growth across the globe. In the US alone, the Consumer Tech industry grew by 9.6% in 2021, indicating a leveling of new technologies by the market, related to smart devices - from 2 in 1 notebook of laptop computing devices, to 4K Ultra HD TVs, wireless headphones, internet enabled or smart TVs, home video game consoles, and smart light bulbs. In Europe, a significant forecasted growth in 2022 is triggered by tablets, smart watches, Laptops, TVs and smart phones.

Enhanced connectivity, prompted by 5G, will lead to a significant growth in the digital economy, namely Industrial Internet of Things (IoT), Enterprise adoption, increased Cloud Infrastructure via digital transformation, sustained remote work, just to name a few. The emergence and growth of Artificial Intelligence (AI) use cases and applications derived from the migration of the core AI innovations (Machine Learning, Computer Vision, etc.) to Transformative AI applications (Autonomous Systems, Advanced 5G/6G Connectivity, Food Technology, Health) and more.

There is a lot of discussion on the emergence of the Metaverse. What, how and when the artificial world will connect with the physical world to improve life and work. The top growth trends to watch in 2022 are expected to occur in Transportation (Electric and Autonomous Vehicles, Micro-mobility), connectivity (5G, Mobile Everywhere always connected and beyond), Sustainable Technologies (Alternative Power Sources, Smart Homes, Smart Cities, Food Tech), Digital Health (Wearable Therapeutics, Mental Health) and Space Technology (Commercial Applications, Communication and possible Tourism). Mobility (Smart and Electric) open new opportunities for new engineering areas smart mobility and urban air mobility.

All of the above are sustained by five pillars that require robust and innovative thermal management design and technologies: 1) Ubiquitous Compute; 2) Pervasive Connectivity; 3) Cloud to Edge Infrastructure; 4) Artificial Intelligence and 5) Green/Clean Energy. These create greater opportunities for our thermal and mechanical engineers, technologists, and scientists across the globe, as the cooling requirements become more critical than ever before. All the incredible advancements in graphics, PC compute and gaming, mobile and connectivity devices, automated driving solutions, advanced health and life sustaining solutions require a shift in the way we think and cool the New Digital World. It is up to each and all of us to make significant contributions to these new areas, working together with our creative and talented electronics cooling community!

We hope that you enjoy our publication and we encourage you to work with our thermal community members, to contribute new innovations in our field, push the limits to develop new exciting thermal management concepts. Tell us about it and contribute to our publication through exciting and educational articles that we strive to align with today's great innovations in various technology areas. I wish you a fruitful and healthy New Year 2022. Stay healthy, happy, inspired and creative!

Thank you and happy reading!

Victor Chiriac

TECHNICAL EDITORS SPOTLIGHT
Meet the 2022 *Electronics Cooling®* Editorial Board

VICTOR CHIRIAC, PhD | GLOBAL COOLING TECHNOLOGY GROUP
Associate Technical Editor

A fellow of the American Society of Mechanical Engineers (ASME) since 2014, Dr. Victor Adrian Chiriac is a co-founder and a managing partner with the Global Cooling Technology Group since 2019. He previously held technology/engineering leadership roles with Motorola (1999-2010), Qualcomm (2010 - 2018) and Huawei R&D USA (2018 - 2019). Dr. Chiriac was elected Chair of the ASME K-16 Electronics Cooling Committee and was elected the Arizona and New Mexico IMAPS Chapter President. He is a leading member of the organizing committees of ASME/InterPack, ASME/ IMECE and IEEE/CPMT ITherm Conferences. He holds 19 U.S. issued patents, 2 US Trade Secrets and 1 Defensive Publication (with Motorola), and has published over 107 papers in scientific journals and at conferences.

▶ vchiriac@gctg-llc.com

GENEVIEVE MARTIN | SIGNIFY
Associate Technical Editor

Genevieve Martin (F) is R&D manager for thermal & mechanics competence at Signify (former Philips Lighting), The Netherlands. She is working in the field of cooling of electronics and thermal management for over twenty years in different application fields. From 2016 to 2019, she coordinates the European project Delphi4LED (3 years project) dealing with multi-domain compact model of LEDs. She served as General chair of Semitherm conference and is an active reviewer and technical committee in key conferences Semi-Therm®, Therminic, Eurosime.

▶ genevieve.martin@signify.com

ALEX OCKFEN, P.E. | META
Associate Technical Editor

Alex Ockfen is a simulation engineer at Meta (formerly Facebook), providing technical leadership for thermal and structural design of consumer electronics products. He held previous positions at Raytheon where he obtained experience in thermal management and electronics cooling of a wide range of aerospace and defense applications. He has more than 10 journal and conference publications, is an inventor on multiple patents, is a professional mechanical engineer, and is currently serving as vice program chair of the SEMI-THERM conference.

▶ alex.ockfen@fb.com

ROSS WILCOXON | COLLINS AEROSPACE ADVANCED TECHNOLOGY
Associate Technical Editor

Dr. Ross Wilcoxon is a Technical Fellow in the Collins Aerospace Advanced Technology group. He conducts research and supports product development related to component reliability, electronics packaging and thermal management for communication, processing, displays and radars. He has more than 40 journal and conference publications and is an inventor on 30 US Patents. Prior to joining Rockwell Collins (Now Collins Aerospace) in 1998, he was an assistant professor at South Dakota State University.

▶ ross.wilcoxon@collins.com

COOLING EVENTS
News of Upcoming 2022 Thermal Management Events

MAR
07-10

18TH ANNUAL DEVICE PACKAGING CONFERENCE (DPC 2022)
We-Ko-Pa Resort and Conference Center
The 18th Annual Device Packaging Conference (DPC 2022) is a major forum for the exchange of knowledge and provides numerous technical, social and networking opportunities for meeting leading experts across microelectronics assembly and packaging. People who will benefit from this conference include scientists, process engineers, product engineers, manufacturing engineers, professors, students, business managers, and sales & marketing professionals.
Desc. source: electronics-cooling.com
► https://www.imaps.org/device_packaging_conference.php

MAR
20-24

APEC 2022
George R. Brown Convention Center
The Applied Power Electronics Conference (APEC) focuses on the practical and applied aspects of the power electronics business. This is not just a designer's conference; APEC has something of interest for anyone involved in power electronics:
Desc. source: electronics-cooling.com
► https://apec-conf.org/conference/registration/

MAR
21-25
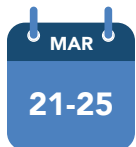
38TH ANNUAL SEMICONDUCTOR THERMAL MEASUREMENT, MODELING AND MANAGEMENT SYMPOSIUM
DoubleTree by Hilton San Jose
The SEMI-THERM thermal symposium is a week full of technical presentations, a keynote presentation, exhibits, a panel discussion and your choice of short courses.
Topics include thermally related challenges and solutions for electronic components from the die to the facility level with applications from consumer electronics to aerospace.
Desc. source: electronics-cooling.com
► https://semi-therm.org/

MAY
10

ThermalLIVE™ SUMMIT
Online Event
The ThermalLIVE™ Summit is a one-day event focused on the latest thermal management breakthroughs, trends, and industry developments. Focused on product innovation and technological advancements, the ThermalLIVE Summit will offer the latest and greatest content, including whitepapers, videos, and product demonstrations.
Desc. source: electronics-cooling.com
► https://thermal.live/

OCT
18-19

ThermalLIVE™ 2022
Online Event
ThermalLIVE™ 2022 is a two-day, free online learning and networking event for engineers to learn about the latest topics in thermal management. Produced by Electronics Cooling, it showcases the newest techniques and products in the industry.
Desc. source: electronics-cooling.com
► https://thermal.live/

thermalLIVE

ThermalLIVE™ SUMMIT: MAY 10

ThermalLIVE™ 2022: OCTOBER 18-19

ONLINE EVENTS

The Largest Thermal Management Events of The Year - Anywhere.

ThermalLIVE™ Summit is a one-day event focused on the latest thermal management breakthroughs, trends and industry developments. With a focus centered on product innovation and technological advancements, the ThermalLIVE Summit will offer the latest and greatest content, including whitepapers, videos, and product demonstrations.

Thermal LIVE™ 2022 is a two-day, free online learning and networking event for engineers to learn about the latest topics in thermal management. Produced by Electronics Cooling, it showcases the newest techniques and products in the industry.

For more information about Technical Programs,
Thermal Management Resources, Sponsors & Presenters

please visit:

www.thermal.live

presented by | **electronics COOLING**

Electric Motor Thermal Management for Green Transportation

Amitav Tikadar, Yogendra Joshi and Satish Kumar

G. W. Woodruff School of Mechanical Engineering, Georgia Institute of Technology

INTRODUCTION

Stringent greenhouse gas-emission legislations have accelerated the electrification of ground and air transportation. Since the electric motor is one of the core components of the electric drivetrain, improving its performance is a key enabler to better performance metrics of an electric drivetrain, i.e., higher power and torque density, better fuel economy (lower \$/mile), and overall drivetrain efficiency. Permanent magnet synchronous motors (PMSM) are broadly used in traction powertrains because of their high power, torque density, and efficiency. However, high heat generation rates in PMSM as a consequence of electromagnetic (EM) losses often limit motor efficiency and longevity by aging the winding wire insulation and premature demagnetization of the magnets. Therefore, proper quantification of heat generation in electric motors and advanced embedded motor cooling techniques remain topics of immense interest. In this article, we discuss an efficient two-way coupled EM and thermal modeling framework for electric motors. By utilizing the developed modeling framework, we present two advanced thermal management techniques, namely embedded circular cooling channel within the stator core and direct winding heat exchanger (DWHX), and emphasize their impact on peak temperature and thermal performance of an electric motor.

For low power electric machines, air cooling is typically used, whereas high power density electric motors typically require liquid cooling to tackle high heat loads [1]. Typically, in automotive and industrial machines, closed-loop liquid cooling via an external cooling jacket around the motor stator is employed [2]. However, jacket cooling (JC) technology often suffers from poor heat extraction from the windings to the external coolant because of the high overall thermal resistance between the windings and the coolant.

In contrast to jacket cooling, which is employed externally to the stator, cooling channels can be employed in the stator and rotor cores. This cooling technique has been adopted by multiple industries. For example, Rolls Royce implemented circular channels to the stator core of a PMSM motor [3], while Siemens AG also designed stator cooling channels adjacent to the windings for high power generators [4]. Rectangular channels were

Amitav Tikadar

Amitav received his B.S and MS degree in mechanical engineering from Bangladesh University of Technology (BUET), Bangladesh and University of South Carolina, USA, in 2015 and 2019, respectively. He is currently pursuing his PhD degree in mechanical engineering at Georgia Institute of Technology, USA. His research interest focuses on electric machine thermal management, micro-scale heat transfer, and machine learning.

Yogendra Joshi

Yogendra is Professor and John M. McKenney and Warren D. Shiver Distinguished Chair at the G.W. Woodruff School of Mechanical Engineering at the Georgia Institute of Technology. He is an elected Fellow of the ASME, the American Association for the Advancement of Science, and IEEE.

Dr. Satish Kumar

Dr. Kumar is currently Professor in George W. Woodruff School of Mechanical Engineering at Georgia Tech. Kumar received his Ph.D. in Mechanical Engineering and M.S. degree in Electrical and Computer Engineering from Purdue University, West Lafayette 2007; and B.Tech. degree in Mechanical Engineering from the Indian Institute of Technology, Guwahati in 2001. He is an elected Fellow of the ASME and author or co-author of over 100 journal or conference publications.

implemented for cooling the Tesla Model 3 motor [5]. However, cooling channels embedded within stator laminations can alter the magnetic flux path by imposing extra reluctance. To overcome the limitations of the aforementioned cooling techniques, Semidey and Mayor [6] proposed a water-cooled direct winding heat exchanger (DWHX) concept to extract heat directly from the windings. DWHX dramatically reduces the thermal resistances between the winding and the coolant, and hence significantly higher current density can be achieved while operating within the insulation's thermal limit.

Building an experimental setup and performing experiments based on the analytical expressions for advanced cooling design and sizing are not economically viable and cannot guarantee optimal cooling performance. Therefore, numerical simulations can play a critical role in the early stage of the co-design of electric motors. Typically, lumped parameter thermal network (LPTN) and computational fluid dynamics/heat transfer (CFD/HT) are used for electric motor thermal performance analysis. Although EM and thermal performance of electric machines are strongly dependent on each other, most of the previous studies have not considered the effects of the cooling strategy on EM performance because of the high computational cost. Therefore, there is a need for an efficiently coupled EM and thermal simulation technique.

RESULTS AND DISCUSSION

In this article, we present a two-way coupled EM and CFD/HT modeling framework to characterize the overall performance of a jacket-cooled BMW i3 motor. *Figure 1* illustrates the front view of a conventional jacket-cooled BMW i3 motor having a slot/pole ratio of 72/12. The stator lamination diameter, stator bore, slot depth, shaft diameter, and axial lamination length are 240.9 mm, 179.8 mm, 21.5 mm, 60.0 mm, and 130.0 mm, respectively. To reduce the computational cost, a single rotor pole and the corresponding stator configuration have been considered as the computational domain for the EM and 3D CFD/HT simulations by realizing angular and axial symmetry (see *Fig. 1* (b-c)). Additionally, thermal contact resistances and radiation heat transfer has been neglected in the CFD/HT model, and liquid cooling has been simulated as a convective boundary condition on the stator outer surfaces.

Figure 2 (a) and (b) outline the one-way and two-way coupled EM and thermal modeling frameworks. In the conventional one-way coupled algorithm, EM losses are calculated using pre-defined temperatures. Afterwards, all calculated losses are transferred to the CFD/HT model to compute motor temperatures for the pre-defined heat transfer coefficient. In contrast, in the two-way coupled framework, motor temperatures calculated from the CFD/HT model are fed back to the EM model. Motor loss components are then recalculated using the updated temperatures. Since EM and CFD/HT models are linked via the motor temperatures, iterations have been carried out until the maximum temperature difference between volume average temperature of the winding/stator/rotor/magnet at i+1th and ith iteration are less than 0.5°C [7].

(a)

(b)

(c)
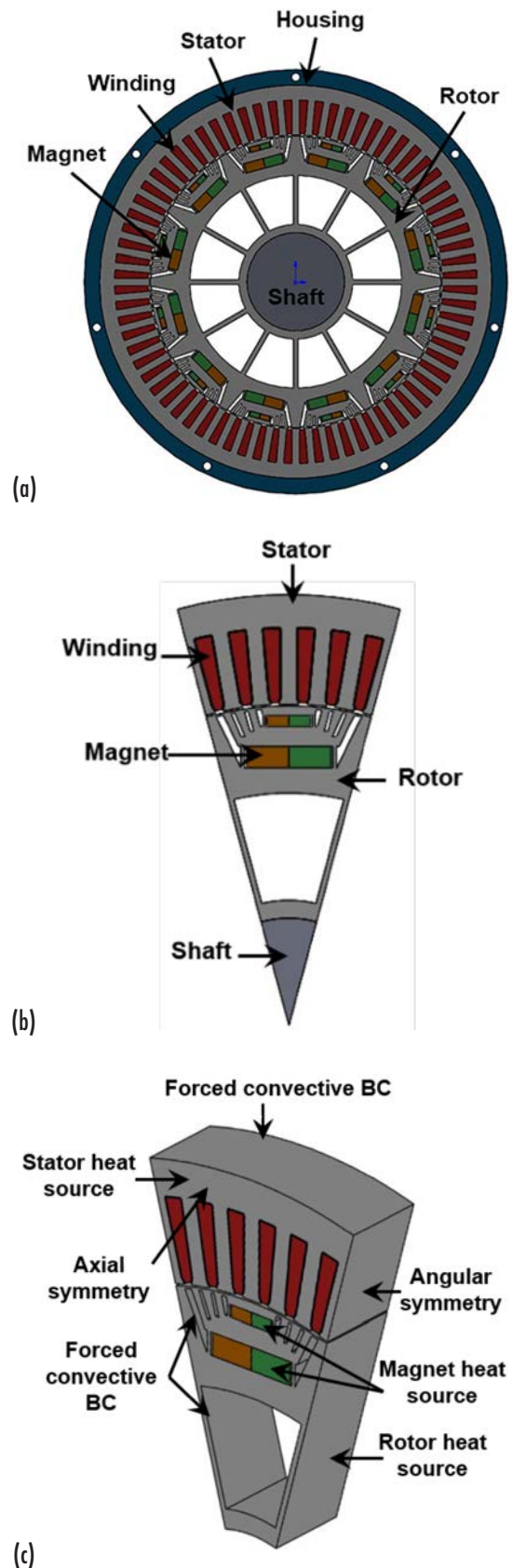
Figure 1: (a) Front view of a 125kW BMW i3 motor and computational domain for (b) 2D electro-magnetic and (c) 3D CFD/HT simulation.
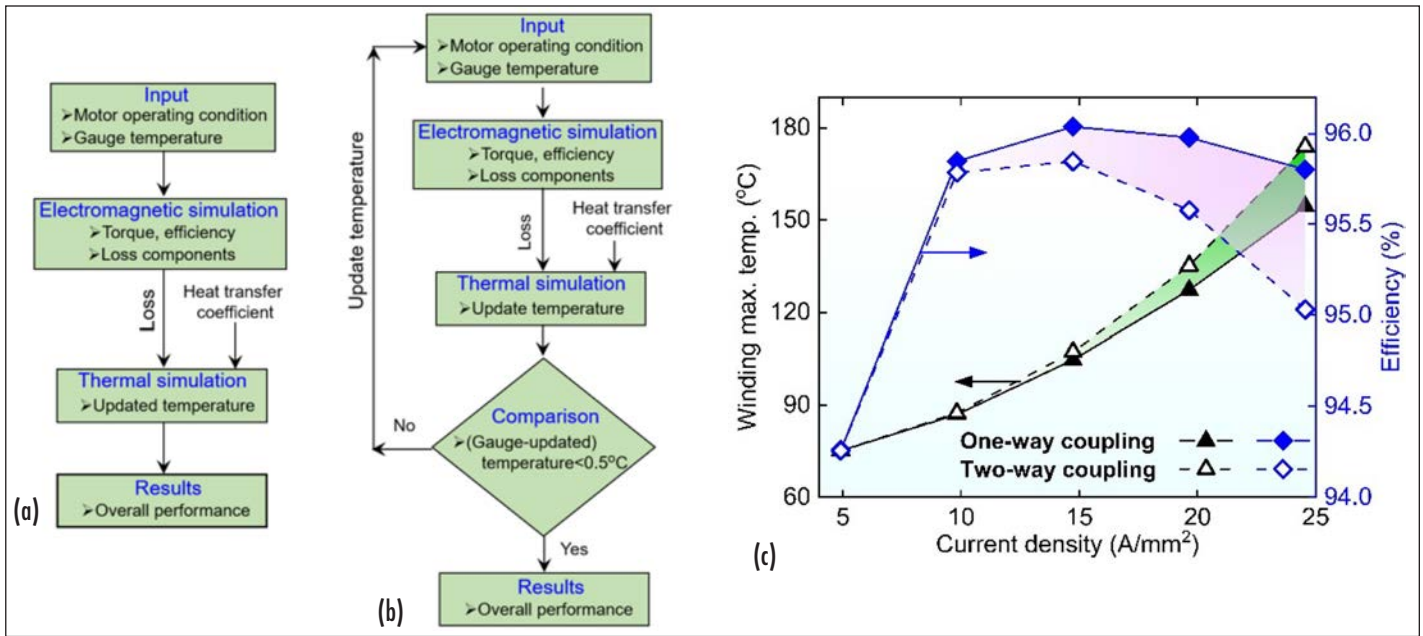
Figure 2: (a) One-way and (b) two-way coupling framework for EM/thermal modeling, (c) Comparison between one and two-way coupling algorithm as a function of current density while maintaining a constant speed of 4,500 rpm and convection heat transfer coefficient of 5,000 W/m²K.

Figure 2 (c) presents the comparison between one and two-way coupled EM and thermal modeling algorithms. At higher current density, the one-way coupling algorithm under-predicts the winding temperature and consequently over-predicts the motor efficiency, compared to the two-way coupling algorithm. The two-way coupling algorithm accounts for increases in the motor temperature, which adversely affect the winding resistance and magnetic flux. These eventually increase copper and core losses, and resulting in higher winding temperature and lower efficiency.
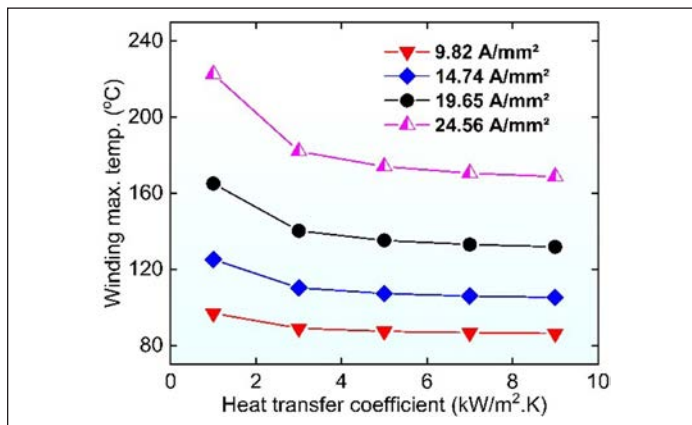
Figure 3: Maximum winding temperature vs. convection heat transfer coefficient for different current densities, while maintaining a constant shaft speed of 4,500 rpm and considering 70ºC as constant fluid temperature.

To assess the effect of convective resistance in the case of jacket cooling, we conducted a parametric study of coolant flow rate through the jacket housing/heat transfer coefficient at the stator outer wall. *Fig. 3* shows that winding temperature gradually reduces as the heat transfer coefficient increases, especially at higher

current densities. This can be attributed to the reduced convective resistance between the motor housing and coolant as the heat transfer coefficient increases. However, beyond a threshold value of heat transfer coefficient of ~5,000 W/m²K, the temperature slope flattens, indicating conduction resistance dominance. In other words, beyond that threshold value of the heat transfer coefficient, motor thermal performance is mainly determined by the conduction resistance between the heat source, i.e., the winding slot and the coolant. Therefore, in order to further enhance the thermal performance of the electric machine, conduction resistance between the winding and the coolant must be reduced.

We used a two-way coupled EM and thermal modeling framework to analyze the effect of implementing circular cooling channels in the stator lamination of a BMW i3 motor (see *Fig. 4* (b)) to directly extract heat from the stator yoke. By integrating cooling channels in the stator back iron, conduction thermal resistance can be significantly reduced by shortening the distance between the windings and coolant. This significantly enhances the thermal performance (see *Fig. 4* (b)) compared to the jacket cooling. At a higher electrical loading of 17.37 A/mm², the circular channels provide significant benefit over jacket cooling, e.g., 14-20°C lower peak temperature for a heat transfer coefficient in the range of 3,000-11,000 W/m²K (see *Fig. 5*). However, directly incorporating cooling channels in the stator may saturate the stator core by introducing additional magnetic flux resistance [8].

The thermal resistance between windings and coolant can be significantly reduced by employing DWHX in the stator slots, as shown in *Fig. 4* (c). The DWHX technique transfers the winding heat loss directly into the coolant, resulting in a significant reduction of the winding-coolant thermal resistance and uniform temperature distribution compared to other cooling techniques (see *Fig. 4* (c)).

For example, by employing DWHX, motor peak temperature can be reduced by ~88-102°C compared to jacket cooling, as shown in *Fig. 5*. Therefore, the integration of DWHX provides a substantial increase in current density within the allowable thermal limit without compromising the thermal integrity. However, a careful design is required to apply DWHX technology in a distributed wound machine and to maintain a high copper fill factor.
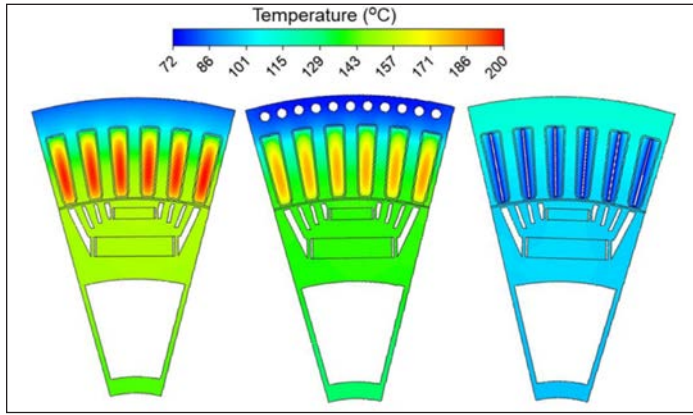
Figure 4: Temperature distributions of (a) jacket cooled, (b) circular channel, and (c) DWHX cooled motor at 4,500 rpm, 17.37 A/mm² current density, 45 EDeg phase advance, and heat transfer coefficient of 5,000 W/m².K.
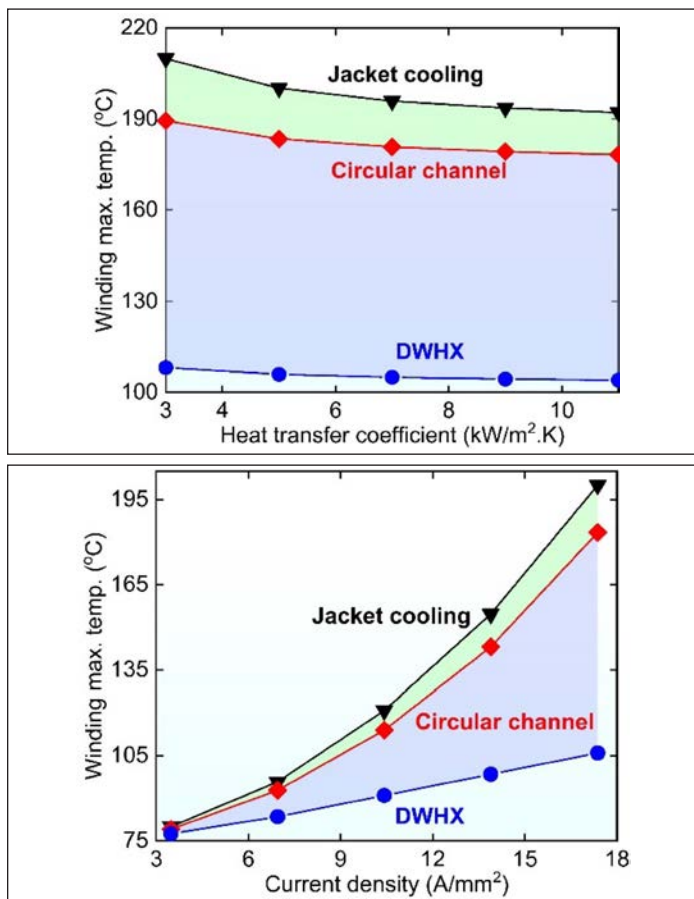
Figure 5: (a) Peak temperature vs heat transfer coefficients at current density of 17.37 A/mm², and b) peak temperature vs current density at heat transfer coefficient of 5,000 W/m².K. For all simulations, motor speed and phase advance were set at 4,500 rpm, and 45 EDeg.

CONCLUSIONS

Since EM and thermal performances of electric motor are dependent on each other, two-way coupled EM-thermal modeling framework can be utilized in the early stage EM design of the electric motor. Although single-phase DWHX can significantly reduce the conduction resistance between the winding and the coolant and offer high current density, DWHX cooling may not be sufficient for next-generation electric ground and air transportation. For ultra-high power density motors, the resistance between the winding and the coolant needs to be eliminated by placing the coolant in direct contact with the winding or by taking advantage of phase-change cooling.

REFERENCES

[1] M. Popescu, D. A. Staton, A. Boglietti, A. Cavagnino, D. Hawkins, and J. Goss, "Modern Heat Extraction Systems for Power Traction Machines—A Review," *IEEE Transactions on Industry Applications,* vol. 52, no. 3, pp. 2167-2175, 2016.

[2] F. JinXin, Z. ChengNing, W. ZhiFu, and E. G. Strangas, "Thermal analysis of water cooled surface mount permanent magnet electric motor for electric vehicle," in *2010 International Conference on Electrical Machines and Systems*, 2010, pp. 1024-1028.

[3] A. J. Mitcham and A. G. Razzell, "Stator Core". Patent 7288870B2, 30 October 2007.

[4] H. Stiesdal, "Generator with a stator comprising cooling channels and method for cooling a laminated stator of a generator". Spain Patent 2415661T3, 26 July 2013.

[5] S. Munro, "Tearing Down Tesla Segment 8: Comparing the Cooling Strategy / Housings of Motors for Tesla Model 3 vs BMW i3," Lean Design, 10 March 2020. [Online]. Available: https://leandesign.com/tearing-down-tesla-segment-8-comparing-the-cooling-strategy-housings-of-motors-for-tesla-model-3-vs-bmw-i3/.

[6] S. A. Semidey and J. R. Mayor, "Experimentation of an Electric Machine Technology Demonstrator Incorporating Direct Winding Heat Exchangers," *IEEE Transactions on Industrial Electronics,* vol. 61, no. 10, pp. 5771-5778, 2014.

[7] A. Tikadar, N. Kumar, Y. Joshi, and S. Kumar, "Coupled Electro-Thermal Analysis of Permanent Magnet Synchronous Motor for Electric Vehicles," in *2020 19th IEEE Intersociety Conference on Thermal and Thermomechanical Phenomena in Electronic Systems (ITherm)*, 2020, pp. 249-256.

[8] A. Tikadar, D. Johnston, N. Kumar, Y. Joshi, and S. Kumar, "Comparison of Electro-Thermal Performance of Advanced Cooling Techniques for Electric Vehicle Motors," *Applied Thermal Engineering,* p. 116182, 2020/10/12/ 2020.

Thermal Management of Integrated Traction Drives in Electric Vehicles

Bidzina Kekelia and Sreekant Narumanchi
National Renewable Energy Laboratory, Golden, CO, USA

This article reviews integration approaches and, by employing finite element analysis (FEA), compares thermal management solutions for the combined electric motor and power electronics systems for electric vehicles. Integration of power electronics into the electric motor helps achieve higher power densities in the electric traction drive systems. The benefit of integration from the thermal management perspective is the potential for using a single-fluid loop instead of two separate cooling systems for the electric machine and the power electronics/inverter.

INTRODUCTION

The number of vehicles on roads with electric propulsion systems is constantly increasing. The global market share of electric and hybrid vehicle sales increased from 2.5% in 2019 to 4.2% in 2020 [1]. According to Deloitte Insights forecasts, by 2030 electric vehicle (EV) market share of new car sales will reach 27% in the United States, 42% in Europe and 48% in China [2].

As demand for EVs is increasing, so is their traction drive power and power density. The push to increase power densities of electric traction drive systems dictates combining the electric motor and power electronics (PE) into one unit to reduce the volume, allowing the unit to be used on multiple vehicle platforms. A single drive unit with fewer interconnecting components also facilitates fast, automated assembly of electric vehicles, driving production costs down and enabling wider adoption of EVs.

Thermal design of today's powerful electric drives is as important as electromagnetic and mechanical design of the electric machine [3]. Integrating power electronics with the electric motor further complicates the thermal management of the combined traction drive system. Two main heat-generation sources in electric vehicles (apart from batteries), often with different cooling requirements and heat removal strategies, are combined into a common space. However, this integration also provides an opportunity for using a single cooling system instead of two separate cooling loops for the electric motor and the power electronics/inverter.

Cooling the electric traction drive in a vehicle can be accomplished by circulating coolant, such as water-ethylene glycol (WEG) or

Bidzina Kekelia
Bidzina is a Senior Research Engineer in the Advanced Power Electronics and Electric Machines (APEEM) Group within the Center of Integrated Mobility Sciences at the NREL. He earned his Bachelor's (Hons) in Mechanical Engineering from Georgian Technical University (1992), M.S. in Renewable Energy (Solar Thermal & PV) from the University of Oldenburg (1999) and Ph.D. in Mechanical Engineering from the University of Utah (2012). After receiving his Ph.D., he worked as a postdoctoral research associate at the University of Utah, developing thermal battery prototypes for electric vehicles. Since joining NREL in 2015, Bidzina's research has focused on exploring novel cooling methods for power electronics and electric drives.

Sreekant Narumanchi
Sreekant is the Group Manager of the Advanced Power Electronics and Electric Machines (APEEM) Group within the Center of Integrated Mobility Sciences at the NREL. He leads a group of 12 researchers focused on thermal, electro-thermal, mechanical and reliability aspects of power electronics and electric machines. He is an ASME Fellow, an IEEE Senior Member, and have published over 80 peer-reviewed journal and conference papers and book chapters. Sreekant is also an Associate Editor for the ASME Journal of Electronic Packaging and an active organizer for InterPACK and ITherm conferences. He received his Ph.D. from Carnegie Mellon University (2003), M.S. from Washington State University (1999), and B. Tech. from Indian Institute of Technology - Kanpur (1997), all in Mechanical Engineering.

oil, through the stator case or internal passages in the motor, thereby removing heat from the components. Another effective method for cooling an electric motor is fluid, such as automatic transmission fluid (ATF), impingement directly on components where heat is generated. This technique avoids the conduction path thermal resistance through the passive stack of other materials present in a water jacket WEG cooling scenario [4], thereby reducing thermal resistance and further lowering key component temperatures. The heat is ultimately rejected to the ambient air.

INTEGRATION TRENDS

In this article, we review the main trends in the integration of electric vehicle propulsion systems and their thermal management solutions. Using publicly accessible scientific literature, published automotive original equipment manufacturer materials, and interactions with other research groups, we identified three main topologies (*Figure 1*):

(1) PE enclosure attached to an electric motor case, eliminating the wire harness, but with separate (often sequential) cooling loops [5,6]

(2) PE radially integrated onto the electric motor case with a shared cooling loop [7,8]

(3) PE axially integrated onto the front/back of the electric motor case with potentially a single-fluid cooling solution (circulating WEG or using ATF jet impingement) [9,10].
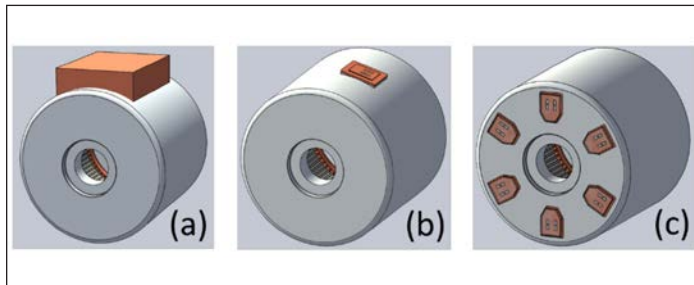
Figure 1. Integration concepts: (a) separate PE enclosure attached to the motor case, (b) PE distributed/mounted radially on the motor casing, and (c) PE integrated axially in the motor front/back plate.

Each of these approaches is implemented with some degree of variation by different manufacturers or research/design teams. Additional overview and integration enabling technologies are reviewed in Chowdhury et al. [11].

THERMAL MODELS AND ANALYSIS

Based on the identified integration trends, simplified computer-aided design (CAD) and thermal models of the integrated traction drives were created. For the electric machine geometry, the 2016 BMW i3 electric traction motor was used. The selection was based on access to its geometry/materials and availability of its detailed benchmarking/losses data [12,13]. The motor losses were used as thermal loads for the thermal simulations. The power electronics model was based on newer silicon-carbide (SiC) metal–oxide–

semiconductor field-effect transistor (MOSFET) dies [14]. These SiC power devices were previously used by Oak Ridge National Laboratory (ORNL) for modeling a simulated control of the BMW i3 motor with a six-phase power module. Thus, their estimated losses/thermal loads were also available [15].

The thermal management strategy for the integration concept shown in *Figure 1a*, with a separate enclosure for power electronics, would resemble one with a completely independent inverter/power electronics and motor. Therefore, radially (*Figure 1b*) and axially (*Figure 1c*) integrated power electronics cooling concepts are of special interest. Hence, respective CAD (see *Figure 2* and *Figure 3*) and thermal models (*Figure 4* and *Figure 5*) were developed and analyzed. For computational efficiency and due to symmetry (PE modules are assumed to be evenly distributed on the outer casing of the motor), only one-sixth of the drive was simulated in the finite element analysis (FEA) simulations.
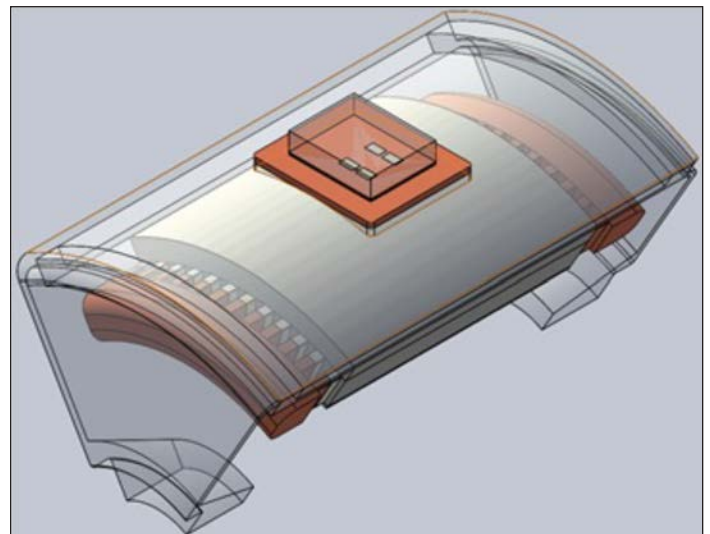
Figure 2. Radially integrated CAD model based on the BMW i3 traction motor and SiC power devices (shared cooling jacket): one-phase power module with one-sixth of the motor.
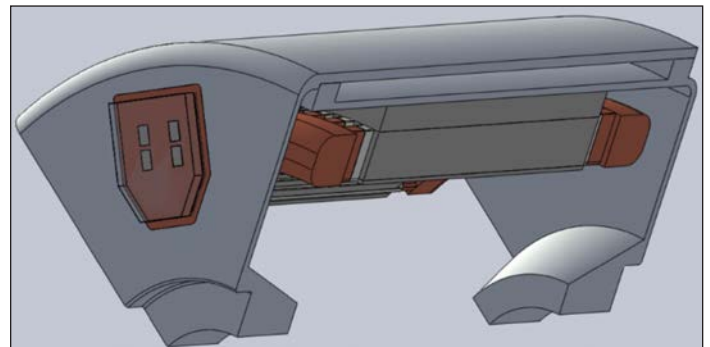
Figure 3. Axially integrated CAD model based on the BMW i3 traction motor and SiC power devices: one-phase power module with one-sixth of the motor.

FEA thermal simulations were carried out with commercially available software [16] by applying thermal loads distributed in the motor components as internal heat generation in the windings, stator yoke, shoe, and teeth. For the power module,

the heat flow was applied to the top surface of the devices, as most of the heat is generated in a junction area in a thin layer close to the top surface of the power device. Coolant temperature was assumed at T_{fluid} =65°C and a convective heat transfer coefficient (HTC) was applied to the internal surfaces of the cooling jacket and the back surface of the power module copper base plate (see *Figure 4* and *Figure 5*), which is exposed to the coolant flow or impinging jets through the openings in the case enclosure. The HTC was varied from h = 20–75,000 W/m²K for each configuration. The HTC range spans from the upper end of air natural convection (20–25 W/m²K) to forced air convection (50–500 W/m²K), forced liquid (WEG) convection with jet impingement toward the higher end (500–50,000+ W/m²K), and phase-change (10,000–75,000+ W/m²K) cooling techniques.
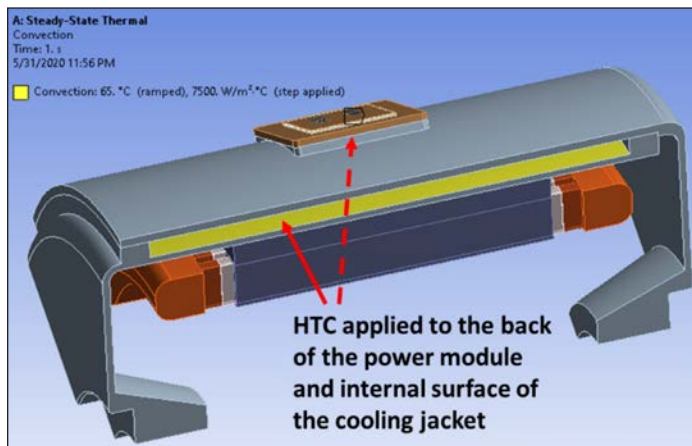
Figure 4. HTC applied to the internal surfaces of the cooling jacket and the back of the power module copper base plate–radially integrated configuration shown.
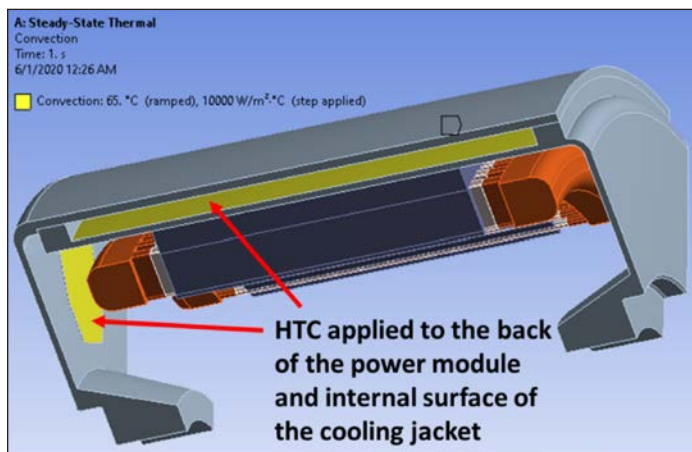
Figure 5. HTC applied to the internal surfaces of the cooling jacket and the back of the power module copper base plate–axially integrated configuration shown.

The integrated power electronics cooling approach for both the radial and axial integration configurations seem reasonable, as the SiC power device temperatures were below key motor component temperatures. For illustration, one set of results for each power integration configuration are provided in *Figure 6* and *Figure 7*.
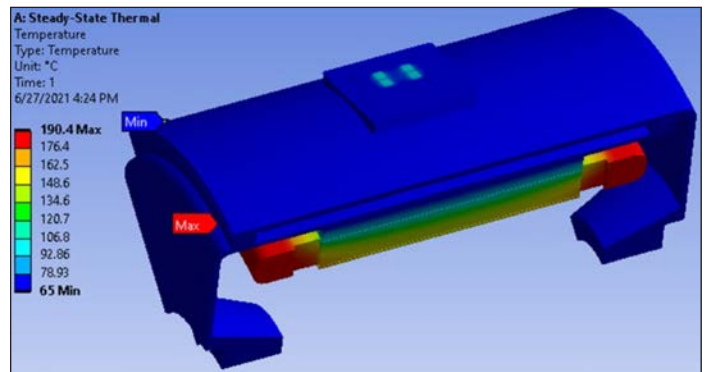
Figure 6. Temperature distribution from the FEA thermal model for the radially integrated power module.
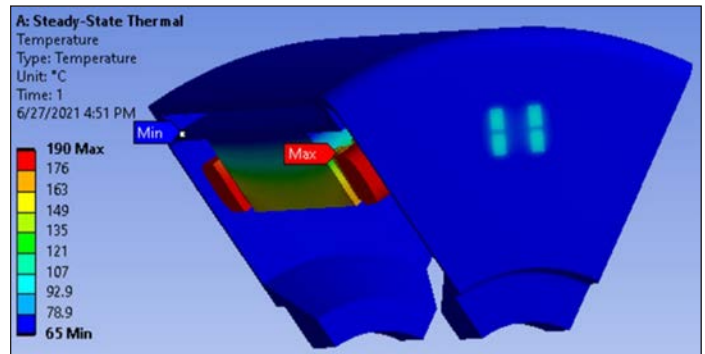
Figure 7. Temperature distribution from the FEA thermal model for the axially integrated power module.

As can be seen from *Figure 6* and *Figure 7*, the highest temperatures (above 150°C) can be observed in the winding end-turns, where a large amount of heat is generated and the thermal path resistance to the cooling fluid is the highest. From a thermal management perspective, the application of ATF or other EV-specific dielectric driveline fluid jet impingement cooling techniques to winding end-turns may benefit overall temperature distributions within the traction drive. Axial integration provides an excellent opportunity for cooling the back side of the power module with ATF or dielectric driveline fluid jets. With a single delivery channel, nozzles could be positioned with jets on one side impinging on the winding end-turns, and jets in the opposite direction cooling the back side of a power module.

In the radial integration configuration, a shared cooling jacket with WEG coolant seems an optimal solution for simultaneous cooling of the power module and electric motor.

CONCLUSIONS

Based on the current market and research publications overview, three main integration approaches were identified for electric traction drives. All three integration approaches yield volumetric and weight savings compared to the traditional traction system solutions. In the baseline case (1), simply bringing power electronics closer and attaching its housing to the electric motor eliminates the interconnection harness between the electric motor and power electronics and reduces the number of required

parts. However, this minimal integration approach most likely requires either separate parallel cooling loops or single sequential coolant flow in the electric motor and the power electronics enclosures. In the radial integration case (2), the cooling options are limited to a shared cooling jacket with circulating WEG, cooling both the electric motor and the power electronics. For the axial integration case (3), both WEG and ATF/driveline fluid jet impingement cooling options are available. If the WEG cooling option is selected, the coolant channels can be integrated into the front/back of the motor casing, converting it to a cold plate, as well as the traditional radial cooling jacket. In the case of ATF/driveline fluid jet impingement cooling, a single channel can deliver fluid both to winding end-turns and the back of the power electronics.

These integration cases show that, with careful design and selection of the appropriate cooling techniques, sufficient cooling can be achieved both for the electric motor and the power electronics with a single, compact thermal management solution.

Tight integration of power electronics into electric motor enables volume, mass and cost savings on their enclosures, interconnections, their cooling systems, and overall number of required parts. This makes electric vehicle propulsion system lighter and more efficient.

REFERENCES
[1] Irle, R., "Global Plug-in Vehicle Sales Reached over 3,2 Million in 2020." EV-Volumes. https://www.ev-volumes.com/country/total-world-plug-in-vehicle-volumes/ (accessed June 27, 2021).
[2] Woodward, M. et al., "Electric vehicles: Setting a course for 2030." Deloitte Insights. https://www2.deloitte.com/us/en/insights/focus/future-of-mobility/electric-vehicle-trends-2030.html (accessed June 27, 2021).
[3] Hendershot, J. R. and Miller, T. J. E., 1994, "Design of brushless permanent-magnet motors." Magna Physics Pub., Oxford, UK.
[4] Bennion, K. and Cousineau, J., 2012, "Sensitivity analysis of traction drive motor cooling," *IEEE Transportation Electrification Conference and Expo (ITEC)*, pp. 1–6.
[5] Bosch, "The modular eAxle drive system." https://www.bosch-mobility-solutions.com/en/products-and-services/passenger-cars-and-light-commercial-vehicles/powertrain-systems/electric-drive/eaxle/.
[6] Krivevski, B., 2019, "Vitesco Technologies Supplies Electric Drive for New Volume-Production Models of Groupe PSA and Hyundai." *Electric Cars Report*, October 16, 2019. https://electriccarsreport.com/2019/10/vitesco-technologies-supplies-electric-drive-for-new-volume-production-models-of-groupe-psa-and-hyundai/.
[7] Kane, M., 2014. "Siemens Integrates Electric Car Motor/Inverter Into Single Unit. *Inside EVs*, November 15, 2014. https://insideevs.com/news/323281/siemens-integrates-electric-car-motor-inverter-into-single-unit/.
[8] Tenconi, A., Profumo, F., Bauer, S.E. and Hennen, M. D., 2008, "Temperatures Evaluation in an Integrated Motor Drive for Traction Applications," *IEEE Transactions on Industrial Electronics*, Vol. 55, No. 10, pp. 4800–4805.
[9] Ullah, S., Winterborne, D. and Lambert, S. M., 2019, "Next-Generation Integrated Drive: A High Power Density Permanent Magnet Synchronous Drive with Flooded Stator Cooling." *J. Eng.*, Vol. 2019, Iss. 17, pp. 4231–4235.
[10] Wang, J., Li, Y. and Han, Y., 2015, "Integrated Modular Motor Drive Design With GaN Power FETs," *IEEE Transactions on Industry Applications*, Vol. 51, No. 4, July–August 2015.
[11] Chowdhury, S., Gurpinar, E., Su, G., Raminosoa, T., Burress, T. A. and Ozpineci, B., 2019, "Enabling Technologies for Compact Integrated Electric Drives for Automotive Traction Applications," *2019 IEEE Transportation Electrification Conference and Expo (ITEC)*, Detroit, MI, pp. 1–8, doi: 10.1109/ITEC.2019.8790594.
[12] Burress, T., 2016, "Benchmarking EV and HEV Technologies," *U.S. DOE Vehicle Technologies Office 2015 Annual Merit Review and Peer Evaluation Meeting*, Washington, D.C. https://www.energy.gov/sites/prod/files/2016/06/f32/edt006_burress_2016_o_web.pdf.
[13] Burress, T., 2017, "Electrical Performance, Reliability Analysis, and Characterization," *2017 U.S. DOE Vehicle Technologies Office Annual Merit Review*, Washington, D.C. https://www.energy.gov/sites/prod/files/2017/06/f34/edt087_burress_2017_o.pdf.
[14] Datasheet from Wolfspeed/Cree SiC die CPM3-0900-0010A. https://www.wolfspeed.com/power/products/sic-bare-die-mosfets/900v-bare-die-silicon-carbide-mosfets-gen3.
[15] Gurpinar, E. and Ozpineci, B., 2018, "Loss Analysis and Mapping of a SiC MOSFET Based Segmented Two-Level Three-Phase Inverter for EV Traction Systems," *2018 IEEE Transportation Electrification Conference and Expo (ITEC)*, Long Beach, CA, pp. 1046–1053, doi: 10.1109/ITEC.2018.8450188.
[16] Ansys Mechanical, Structural FEA Analysis Software. https://www.ansys.com/products/structures/ansys-mechanical.

Breaking Grounds with Generative Design for Two-phase Cooling of Electronic Devices

Dr. Lieven Vervecken, Dr. Joris Coddé, Dr. Roxane Van Mellaert and Dr. Joao Miranda

Diabatix nv, Leuven Belgium

INTRODUCTION

Since the size of electronic components keeps on decreasing, the need for improved heat dissipation on these components keeps increasing. This dichotomy presents thermal engineers with a formidable challenge: how to design smaller coolers that dissipate more heat. Adding to the challenge, the fast-paced evolution of electronics means that the development time for the new cooler designs is shorter and shorter.

This article explores the combination of generative design and advanced two-phase cooling simulation techniques to efficiently create two-phase electronics cooling devices. The article starts with a discussion of the numerical models followed by a brief explanation of the generative design method. Finally, a proof-of-concept design is shown and discussed.

TWO-PHASE COOLING MODELING

Over recent years, computational simulations have become an integral part of the design cycle for new products. The increase of computational power, in combination with the development of more advanced numerical models, enables the simulation of complex problems more accurately and faster than ever before. Adopting simulations during the design cycle greatly increases the efficiency of the development process from both cost and time points of view. When compared to experimental tests, simulations tend to be much more affordable and easily scalable, meaning that a much wider design space can be explored at a fraction of the cost.

When substituting experimental tests with simulations, the accuracy of the latter is key. By definition, simulations rely on models that only approximate physical behavior. As the

Dr. Lieven Vervecken
Dr. Vervecken is CEO and co-founder of Diabatix, a software company specialized in advanced thermal design. Prior to founding Diabatix, Lieven received a PhD in mechanical engineering from the renowned University of Leuven, in the field of numerical simulations. Lieven incorporated his expertise into the advanced A.I. technology that lies at the heart of Diabatix. What started out as a small venture has become a fast-growing SaaS company serving multinationals all over the world. Lieven is lead author of multiple peer-reviewed journal articles and he is an experienced keynote speaker at national and international conferences.

Dr. Joris Coddé
Dr. Coddé co-founder of and R&D engineer at Diabatix. He obtained his master's degree in energy engineering and his PhD in heat transfer modeling at the University of Leuven. As one of the founders of Diabatix, Joris has witnessed first-hand how the company has evolved from a small start-up to a SaaS provider with clients all over the world. From the start, he has been actively contributing to the new technological developments at Diabatix.
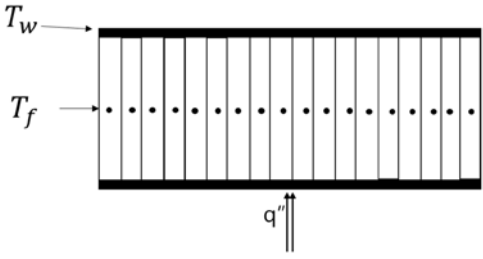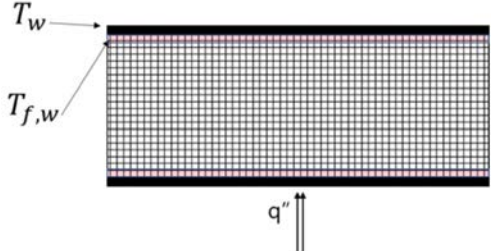
Dr. Roxane Van Mellaert
Dr. Van Mellaert is Head of Operations at Diabatix and she was the first employee to be hired by the founders of the company. She received her master in architectural engineering and her PhD in structural optimization from the University of Leuven. During the course of her PhD, Roxane's research was published in multiple peer-reviewed journals. She started in 2017 as R&D Engineer and gradually climbed her way up to her current function of Head of Operations. As part of the management of Diabatix, she oversees all ongoing development projects related to ColdStream and ensures the proper exploitation of the platform.

Dr. João Miranda
Dr. Miranda joined the Diabatix team in July 2020 as an R&D Engineer. He obtained a Master's degree in Aerospace Engineering at the Instituto Superior Técnico in Lisbon. After moving to Belgium he obtained a PhD in Mechanical Engineering at the Vrije Universiteit in Brussels. Since his start at Diabatix he has been continuously contributing to the development of the ColdStream platform with a focus on improving the Computational Fluid Dynamics simulations. In addition to this, João is in charge of managing all scientific publications by Diabatix.

Table 1: Visual comparison between one-dimensional modeling approach and finite-volume approach	
	One-dimensional approach Solve a one-dimensional equation for the fluid temperature along the channel. Heat transfer is calculated using empirical correlations for the convective heat transfer coefficient.
	Finite-volume approach Solve for the full three-dimensional flow field in the channel. Heat transfer is simulated using an effective thermal conductivity.

complexity of models is often directly related to their performance and computational costs, choosing the correct models becomes a fundamental step in the design procedure. In conjugate heat transfer problems, the simulation of the solid and fluid components can be, to a certain degree, treated independently.

One common approach is to simulate the solid with a thermal resistance model, or more advanced numerical models such as finite elements, and approximate the fluid with a one-dimensional model along the flow channel, as depicted in *Table 1*. In this approach, the heat transfer between the solid and the fluid is calculated as the temperature difference along the channel multiplied by a convective heat transfer coefficient that is typically obtained from Nusselt correlations. The approach is computationally friendly because it avoids the direct computation of coolant behavior. However because the approach ignores local variations of fluid characteristics, such as boundary layers and turbulence, a design obtained using this approach is likely to be sub-optimal.

An alternative approach is to simulate both the solid and the fluid with a three-dimensional simulation code and solve for the full flow field in the channel. In this case, the two-phase flow is fully simulated on a detailed computational grid and the heat exchange between the solid and the fluid depends only on the temperature difference between the solid and the fluid cells adjacent to the wall. While computationally more expensive, the approach results in more detailed insight into the physics of the problem, thus allowing for more accurate results.

Compared to single-phase flows, two-phase flows present a much higher complexity. The interactions between the flow phases and the differences in physical characteristics of each phase make the simulation of a two-phase flow challenging. The simplest hydrodynamic model of a two-phase flow is the homogeneous model. This model postulates that the liquid

and vapor phases are well mixed, move with the same velocity, and are thermodynamically in equilibrium. In essence, the two-phase flow is treated as a single-phase fluid. Alternatively, inhomogeneous multiphase models can be used. These models take into account the velocity slip between the vapor and liquid phases. This requires interface modeling and tracking, which result in a significantly higher computational cost. A comparison between both modeling approaches is given in *Table 2*, for a more exhaustive comparison see [4].

Table 2: Comparison table HEM model and inhomogeneous multiphase model	
Homogeneous Equilibrium Model (HEM)	**Inhomogeneous Multiphase Model**
All phases move at the same velocity	Each phase has its own flow field
There is no interphase mass and momentum transfer	Interphase mass and momentum transfer are considered
The same pressure is shared by all phases	The same pressure is shared by all phases
Same turbulence shared by all phases	Different turbulence for all phases
Phases are in thermodynamic equilibrium	No equilibrium required
Mixture transport equations	Transport equation for each phase

The general equations of multiphase flows consist of three transport equations, for mass, momentum, and energy, along with additional jump conditions at the interfaces between the vapor and liquid phases to close the system of equations. However, using the HEM, the two-phase flow is treated as a single-phase fluid with energy-dependent fluid properties along the channel. This reduces the system of equations to the single-phase Navier-Stokes equations in which the fluid properties are evaluated based on the local flow quality or local vapor fraction.

Regardless of which two-phase model is used, the heat transfer at the solid-fluid interface must be quantified. For this work, a new modeling approach was developed based on the two-phase multiplier concept of Lockhart and Martinelli [1], which imposes that:

$$h = F(G, x, \dots)h_{lo} \qquad (1)$$

Where h is the actual heat transfer coefficient, h_{lo} is the convection heat transfer coefficient when all mass is saturated liquid, which is evaluated through CFD simulation, and the function $F(G,x,\dots)$ is a two-phase multiplier that acts as a correction factor to h_{lo}.

Using a finite-volume, the local heat transfer coefficient between the wall and coolant is computed as

$$h_{lo} = \frac{q''}{T_w - T_{f,w}} = \frac{k_{eff}}{\Delta} = \frac{1}{\Delta}\left(k_f + \frac{\mu_t}{Pr_t}\right)$$

Where k_f is the conductivity of the fluid, μ_t is the turbulent viscosity, Pr_t is the turbulent Prandtl number, typically equal to 0.85, and $T_w, T_{w,f}$ are, respectively, the temperatures at the wall and the fluid next to the wall.

To model the two-phase multiplier, the correlation of Bennett and Chen is applied [5]:

$$F = C\left(\frac{Pr_f - 1}{2}\right)^{0.444}\left(1 + X_{tt}^{-0,5}\right)^{1.78}$$

Where X_{tt} is defined as

$$X_{tt} = \left(\frac{\rho_g}{\rho_l}\right)^{0.5}\left(\frac{\mu_l}{\mu_g}\right)^{0,1}\left(\frac{1-x}{x}\right)^{0,9}$$

An additional scale factor C is introduced to temper the effect of local high quality values.

GENERATIVE DESIGN

Generative design is an automated design process that requires minimal user input and interaction while generating high-performing designs. Generative design techniques explore the design space by iterating between different possible solutions and learning information at each iterative step to converge to an optimal design. From a set of inputs such as design space, objectives, and constraints, the algorithm explores different possible solutions for the problem, evaluates them, and uses the collected information to generate new and possibly better solutions. The cycle repeats until the best possible solution that respects the constraints is found. By evaluating each possible solution with advanced numerical simulations, the optimization algorithm becomes fully autonomous, thus reducing the human interaction in the design cycle to the set-up of the problem and the final design evaluation. To generate new possible solutions at each step of the design process, the information learned from analyzing previous solutions can be used in several different ways. Due to the limited user interaction with the design process, the human bias towards specific or well-known designs is avoided, thus allowing for a true complete exploration of the design space towards a potentially global optimum.

A popular generative design strategy is to apply topological optimization in which a design is generated by optimizing the material distribution in the design space. In broader terms, a part of the coolant space is transformed into a new material, which will define a new design. A major advantage of topological optimization is that it does not depend on an initial design; therefore, the design space can be freely explored and allow for a potentially better final design. In this work, the HEM two-phase model is used in combination with proprietary topology optimization software [2] to generate a high-performing two-phase cooling device. A gradient-based optimization algorithm is applied and manufacturing constraints, such as minimal feature size and other 3D printing restrictions, are enforced via manipulation of the design sensitivities.

CASE STUDY

To demonstrate the feasibility of the proposed design approach, the remainder of the article is dedicated to a case study. The base geometry, shown in Figure: 1, represents a simplified 2-phase cooled heat sink, called the evaporator, that could potentially be used in actively cooled communication satellites. The goal of the study was to minimize the temperature on the heat sources (Equation 2), within a pressure drop constraint (Equation 3), and additional manufacturing constraints for 3D printing.

$$\min \quad J = \frac{1}{A}\int T \, dA, \qquad (2)$$

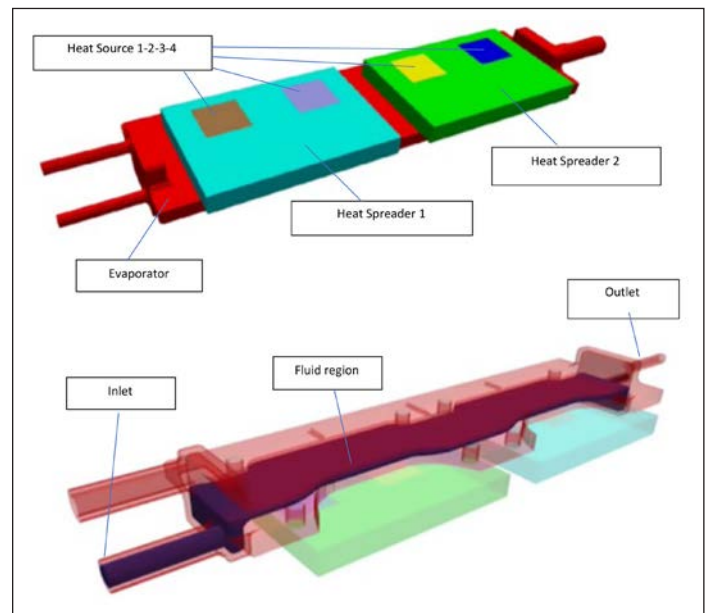$$\text{subject to} \quad P_{in} - P_{out} \leq C \qquad (3)$$

Figure 1: base geometry for the design optimization study

The base geometry for the optimization study is shown in Figure 1. The geometry consists of 4 heat sources that are mounted on two heat spreaders. In turn, the heat spreaders are mounted on the evaporator. For the numerical analysis, the geometry was discretized using a fully hexagonal mesh.

The heat spreaders and the evaporator are both manufactured from aluminum alloys (AL 6061) with a density of 2701 kg/m³ and thermal conductivity of 150 W/mK. A contact conductance of 30 kW/m²K is applied at the interface between the heat spreaders and the evaporator. A total heat dissipation rate of 200W, i.e. 50W per heat source, is imposed. Saturated ammonia is used as the coolant with inlet conditions of 80°C and pressure of 41.42 bar. The properties of ammonia under these conditions are given in *Table 3*. The vapor quality at the inlet is set to 6.7e-5 (or a vapor fraction of 0.1%). The mass flow rate equals 3.33e-4 kg/s. Under these conditions, the quality increases up to 0.6865 at the outlet.

Table 3: two-phase properties of ammonia at 80°C		
	Liquid	**Vapor**
Density [kg/m³]	505.67	33.888
Viscosity [Pa s]	7.798e-3	11.95e-6
Thermal conductivity [W/mK]	0.355	0.04223
Enthalpy [kJ/kg]	600.4	1473.7

The case setup described above is used as input for the generative design cycle. Since a generative design approach is being used, no initial design is required. At every iteration of the design cycle, multiple, full-scale 3D Navier-Stokes equations are solved and the full cycle can take up to 1000 iterations to generate a design. This high computational cost is compensated by the fact that no human interaction is required during the entire design cycle.

(a)

(b)
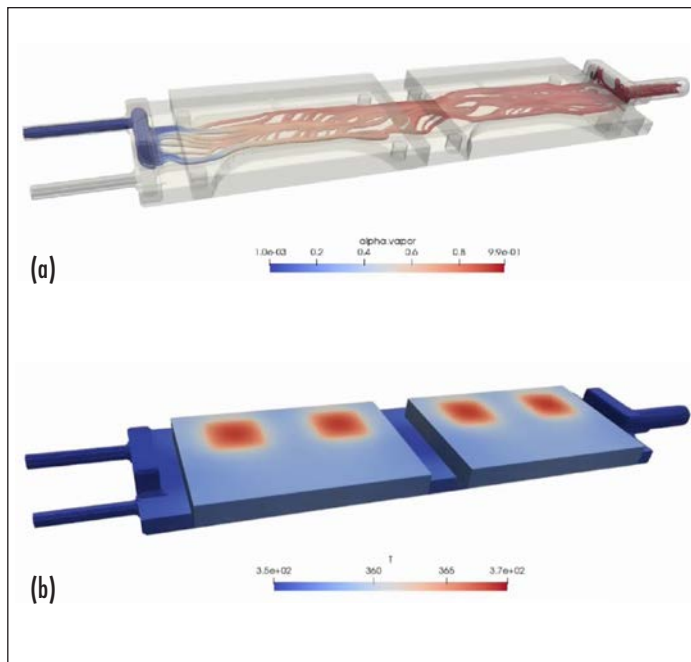
Figure 2: AI design with (a) alpha.vapor the local vapor fraction; (b) evaporator temperature.

The final design is shown in Figure 2 (a) in which the fluid channels are colored according to the local vapor fraction. The evolution of the temperature is shown in Figure 2(b). The optimization searches for a balance between low and high heat transfer in large and small channels at the cost of a low and high-pressure drop. This explains why the design is different under each cooling cell: there is a difference between the fluid entering the regions below each cooling cell, and a difference in flow properties such as density, quality, and viscosity, which all affect the pressure drop. To evaluate the performance of this component and the effectiveness of the optimization, the evaporator was built and tested under laboratory conditions that demonstrated a 15% performance increase compared to a conventional design, constructed from a series of parallel channels (see Figure 10 in [3] for the design). The experimental analyses were performed by the NLR institute, see [3] for more details on the experimental setup and the test procedures.

CONCLUSION

This work demonstrates that generative design can be used to design a two-phase evaporator cooling system with minimal human input or interaction. A fully three-dimensional solid and fluid domain model, combined with an advanced interface heat transfer model based on a two-phase multiplier concept, was used to accurately model the physical behavior of the system. A case study demonstrated that the cooling could be improved up to 15% without affecting pressure drop, manufacturing cost, or cost of the device.

ACKNOWLEDGMENTS

REFERENCES

[1] Maqbool, M.H., 2012. Flow boiling of ammonia and propane in mini channels (Doctoral dissertation, KTH Royal Institute of Technology).
[2] Diabatix ColdStream©, https://coldstream.diabatix.com
[3] Van Gerner, H.J., 2021. Preliminary design of a mechanically pumped cooling system for active antennae, 50th International Conference on Environmental Systems, ICES-2021-002.
[4] Todreas, N.E. and Kazimi, M.S., 2021. Nuclear systems volume I: Thermal hydraulic fundamentals. CRC press.
[5] Ghiaasiaan, S. M., 2008, "Two-phase flow, boiling, and condensation." Conventional and miniature systems

Machine Learning Optimization to Boost the Effectiveness of Phase Change Material (PCM)-Based On-Chip Passive Thermal Management

Dr. Amy Marconnet and Meghavin Bhatasana
Purdue University

INTRODUCTION

Although miniaturization of electronic components has helped advance computing power and accelerated technology development, it has increased power densities and exacerbated the already challenging issue of electronics cooling at the component level. Continuous operation at high temperatures degrades functionality and reduces long-term reliability of electronic devices. As a result, the computational power of these devices is often throttled to prevent such damage. Phase change material (PCM) embedded heat sinks, attached to chips, can increase the thermal capacitance of the system to enable longer periods of operation at full power before throttling or shut-off is required to prevent damage. However, the numerous materials between the heat source and the PCM-laden heat sink limit their effectiveness. Embedding the PCM at the silicon die level, close to the heat source, reduces the resistance pathways associated with chip packaging and traditional bulk PCM-laden heat exchangers. The proximity of the heat source to the PCM (or "thermal capacitor") allows for the thermal manage-ment of transient heat loads and hotspot mitigation. Another important benefit of this embedded PCM strategy is that it provides a compact and passive cooling solution. This is ideal for mobile applications, which require cooling solutions that do not increase the package dimensions. Strategic placement and choice of the PCM (including its melting point and thermophysical properties) also reduce fluctuations in the hotspot temperatures for transient power cycles via the cyclic melting and freezing of the PCM. Here we leverage machine learning tools to enable computationally-efficient optimization of the system performance. Specifically, we evaluate the merits of embedding the PCM directly within the silicon chip through computational modeling and machine learning optimization.

SYSTEM CONFIGURATION

Figure 1 illustrates the silicon-based device of interest. Heaters mimic the power generated in electronic devices and channels or pockets are etched in the silicon to embed the PCM within the silicon device. They are passivated with an oxide or alumina

Dr. Amy Marconnet
Amy Marconnet is an associate professor of Mechanical Engineering and a Perry Academic Excellence Scholar at Purdue University. She received a B.S. in Mechanical Engineering from the University of Wisconsin – Madison in 2007, and an M.S. and a PhD in Mechanical Engineering at Stanford University in 2009 and 2012, respectively. Her dissertation focused on thermal phenomena in nanostructured materials. She then worked briefly as a postdoctoral associate at the Massachusetts Institute of Technology, before joining the faculty at Purdue University in August 2013. She was promoted to associate professor with tenure in August 2019. Her research group focuses on heat transfer and energy conversion.

Meghavin Bhatasana
Meghavin Bhatasana received his B.S degree in mechanical engineering from Purdue University in 2019. He is currently pursuing his PhD degree in mechanical engineering at Purdue. His research interest focuses on the use phase change materials and semiconductor fabrication techniques for thermal management of consumer and high-power electronics.

layer. Thermal resistances (R_{ja}) between the external surface of the device are representative of the conduction and convection pathways from these surfaces to ambient. To emulate transient heat fluxes representative of devices in operation, the heat generation is modeled as a periodic square wave with an on/off time of 0.5 s.

Thermal analysis is performed using a MATLAB-based simulation tool developed by the Army Research Lab called ParaPower [1]. It utilizes an implicit Euler finite difference scheme integrated with a 3D thermal resistance network to quickly compute the temperature evolution of the electronics module. ParaPower is noted to be >100 times faster than commercial finite element analysis (FEA) packages while ensuring reasonable accuracy (<2°C) [2].
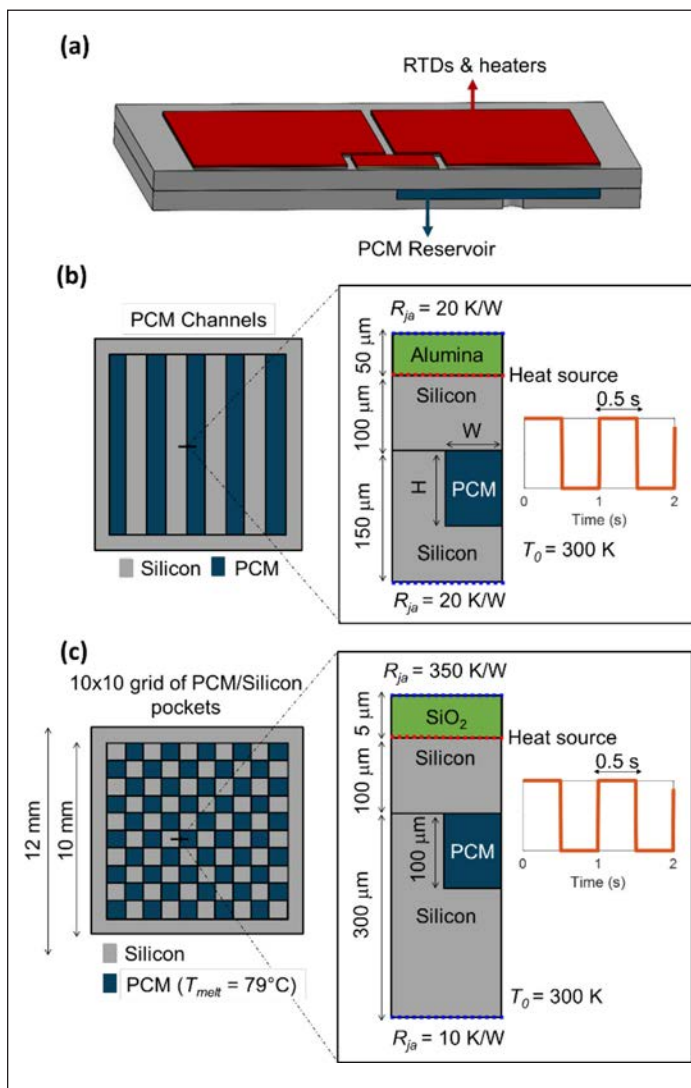

Figure 1: Overview of the device geometry and thermal conditions including (a) a schematic of the PCM-embedded chip geometry including resistive heaters, the silicon chip, and PCM reservoir and details of the geometries used for (b) 2-D and (c) 3-D optimizations. The key differences are the boundary conditions and the thickness of the sealing silicon layer. The insets in b-c illustrate the cross-section of the chip, as well as the boundary conditions and heat source considered in this study.

Here, two metrics are defined to quantify the effectiveness of the embedded PCM cooling strategy:

1. T_{o-max}: Overall maximum chip temperature (across all time steps)
2. T_{osc}: Magnitude of the oscillations in the transient maximum chip temperature $T_{max}(t)$ at quasi-steady state

Note that at a particular instant in time, the transient maximum chip temperature is referenced as T_{max}, while T_{o-max} corresponds to the maximum temperature across all simulated timesteps.

MACHINE LEARNING TOOLS

Machine learning encompasses algorithms and tools that enable computers to learn methods and understand datasets without being explicitly programmed to do so. Machine learning has expansive usage in society. On a daily basis, people interact with machine learning algorithms through Google's search engine, Netflix's show suggestions, and automatic chatbots. They are also used extensively behind the scenes in self-driving technology, medical imaging and diagnostics, mail sorting, and stock trading [3].

To identify the best configuration of the PCM within the chip, we use a popular evolutionary algorithm, called a genetic algorithm (GA). The GA solves optimization problems based on the concept of natural selection. After generating a randomized population set, it selects the best performing individual solutions and evolves them (by crossing over properties and introducing mutations) cyclically until an optimized solution is found. The optimization algorithm can be coupled directly to ParaPower. We use this approach for both the parallel PCM channels (simplified to a 2D geometry, see *Figure 1b*) and for the grid-based structure optimization (see *Figure 1c*). More details about GAs can be found in *Ref. [4]*.

To increase the computational efficiency for the optimization of the parallel PCM channels, we make use of artificial neural networks (ANNs) as surrogate models. Specifically, data from the ParaPower (PP) model is used to train computationally efficient ANNs that are later used for parameter optimization. An accurate ANN enables rapid thermal analysis and, in turn, enables rapid optimization. They are based on the concept of biological neural networks in brains and consist of several processing layers that are interconnected via nodes (called neurons). These layers can be broadly classified into 3 layers: the input layer, the hidden layer(s), and the output layer. The input layer receives information from the user and processes it to the hidden layers, which then process it to the output layer. Any time a layer transmits data to the subsequent layer, it introduces a non-linearity using an 'activation function'. ANNs are robust and have the potential to accurately model non-linear relationships between independent and dependent variables. For more details on ANNs, we refer the reader to *Ref. [5]*.
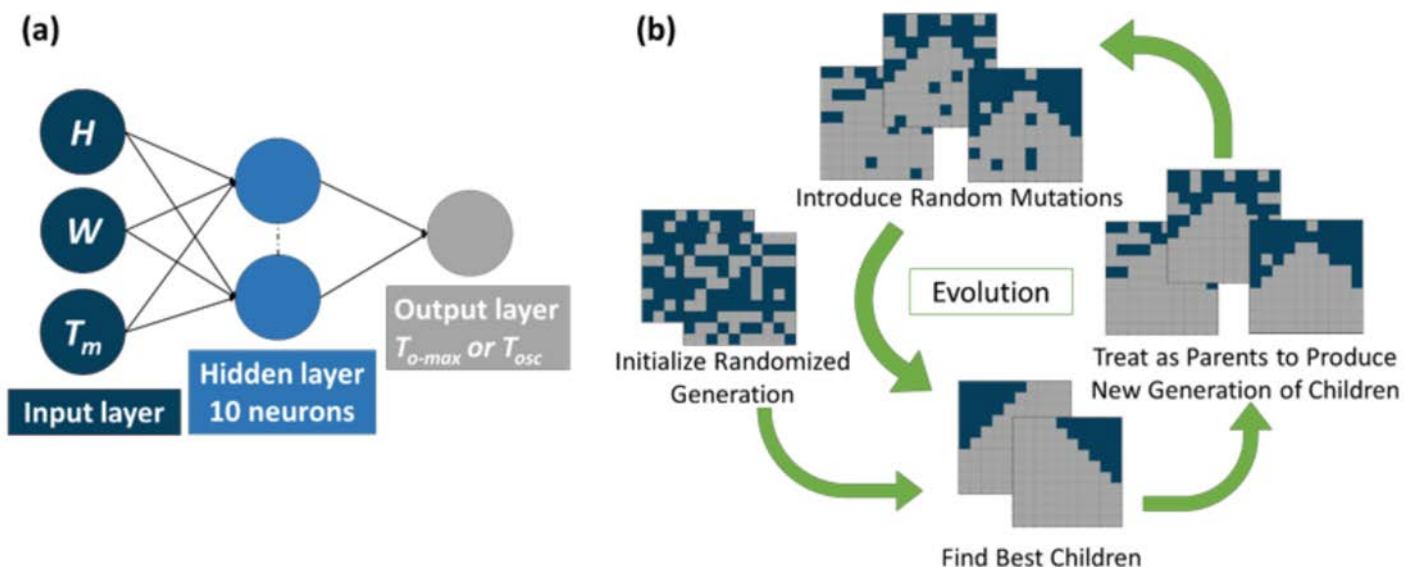
Figure 2: (a) Illustration of the ANN architecture used to predict $T_{o\text{-}max}$ or T_{osc}. The input layer takes height (H), width (W) and the PCM melt temperature (T_m) as inputs and processes them to the single hidden layer with 10 neurons. Here, a Tan-Sigmoid activation function introduces non-linearity. The data then passes over the output layer to predict either $T_{o\text{-}max}$ or T_{osc}. (b) Visual representation of the GA for grid based PCM geometry. When the GA is used with the ANN, the GA cycles between numerical inputs for H, W and T_m.

EMBEDDED COOLING OPTIMIZATION: PARALLEL CHANNELS

First, we optimize a 2-D geometry consisting of parallel channels of PCM (see *Figure 1b*). We explore a multi-parameter optimization of the channel geometry and PCM melt temperature (other thermophysical properties are fixed since they must simply be maximized).

We consider two optimization strategies for this study:

1. **Direct optimization** where the genetic algorithm is directly coupled to ParaPower (GA+PP).
2. **ANN assisted optimization** where the genetic algorithm is integrated with a neural network (GA+ANN). The ANN is built using training data generated with ParaPower and is validated using a separate dataset of 500 cases. The R^2 of the ANN with respect to this testing dataset is reported here. Note that the results shown here for this strategy report the average of ten different runs. Once we generate the data, the ANN is trained ten times with random distributions of the training, validation, and test subsets. Each of these 10 ANNs is then paired to the GA. After the data set generation, the ANN training and GA prediction takes about ~10 seconds.

COMPARISON BETWEEN THE ANN AND DIRECT OPTIMIZATION

We consider the optimization of the PCM melt temperature and the height and width of the PCM channels. The other PCM properties were fixed to that of Alloy 174, which is a metallic composite that melts at 79°C. A parametric sweep for this study would have taken about 28 days, whereas the machine learning strategies generated effective results within 3 hours. Results of the optimization studies are shown in *Table 1*.

When optimizing for minimizing the amplitude of the temperature oscillations T_{osc}, the GA directly integrated with ParaPower (GA+PP) identified filling the entire layer with PCM with a melt temperature of 77°C. The channels occupying the entire available volume may be in part due to the uniform heat source. For minimizing the overall maximum temperature $T_{o\text{-}max}$, the strategy predicts the same optimal melt temperatures but leaves a thin silicon channel for conduction.
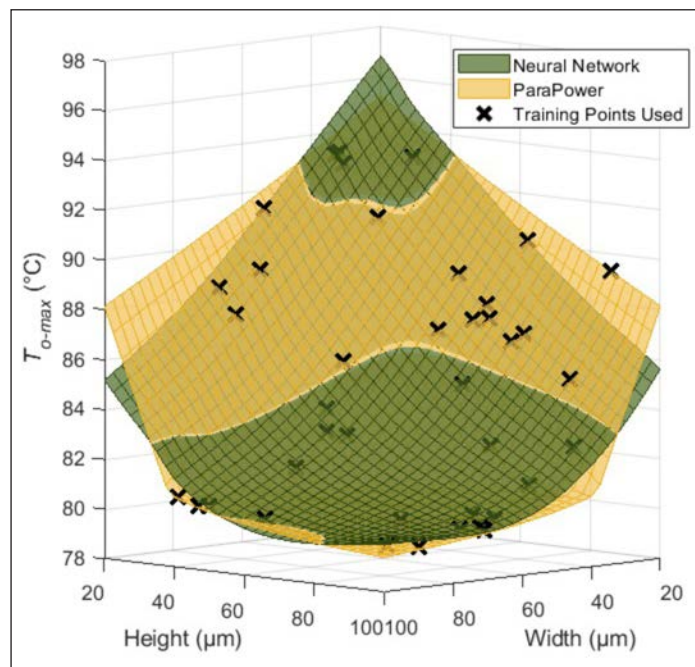

Figure 3: $T_{o\text{-}max}$ predictions by a NN (shown in yellow) alongside ParaPower predictions (shown in green). The NN prediction have a distinct minimum at a height of 100 μm and width of 75 μm that likely accounts for differences in predicted optima.[1]

Table 1: Optimized PCM channel height, width, and melt temperature as well as the required computational time for different optimization strategies									
Strategy	Computational Time (hrs)	Optimizing $T_{o\text{-}max}$			Predicted $T_{o\text{-}max}$ (°C)	Optimizing T_{osc}			Predicted $T_{o\text{-}max}$ (°C)
		H (μm)	W (μm)	T_m (°C)		H (μm)	W (μm)	T_m (°C)	
GA+PP	2.5 ($T_{o\text{-}max}$) + 2.9 (T_{osc})	100	99	77	79	100	100	77	3
GA+ANN	4.5	95	76	78	80	96	91	77	4

Table 2: Trends in NN accuracy and GA predicted optimums for T_{osc} and $T_{o\text{-}max}$[1]											
Computational Time (hrs)	Training Data Size	R^2	Optimizing $T_{o\text{-}max}$			Predicted $T_{o\text{-}max}$ (°C)	R^2	Optimizing T_{osc}			Predicted T_{osc} (°C)
			H (μm)	W (μm)	T_m (°C)			H (μm)	W (μm)	T_m (°C)	
0.06	30	0.37	84	69	77	87	0.52	97	84	81	17
0.08	40	0.50	93	74	82	84	0.39	92	83	82	22
0.09	50	0.62	89	80	73	83	0.58	92	83	82	18
0.19	100	0.90	88	83	79	81	0.89	87	93	77	8
0.28	150	0.96	78	89	79	81	0.95	91	89	77	5
0.47	250	0.97	91	89	79	80	0.96	92	85	77	6
0.95	500	0.98	84	94	78	80	0.98	94	90	77	4
1.89	1000	0.98	94	88	78	80	0.99	94	89	77	6
3.78	2000	0.99	91	93	78	80	0.99	92	83	77	6
4.50	2380	0.99	95	76	78	80	0.99	96	91	77	4

[1] *Adapted and reprinted from Applied Thermal Engineering, Bhatasana and Marconnet, Machine-Learning Assisted Optimization Strategies for Phase Change Materials Embedded within Electronic Packages, Copyright (2021), with permission from Elsevier.*

The ANN-assisted strategy predicted a similar trend of having almost filled PCM channels and a melt temperature of 77°C when optimizing T_{osc}. However, it converged on a melt temperature of 78°C and a channel width that is lower than the upper width boundary for $T_{o\text{-}max}$. This may be due to the ANN inaccuracy near the optimized data range. To explore this, *Figure 3* compares the NN model predictions $T_{o\text{-}max}$ to the ParaPower results over a range of heights and widths with a fixed PCM melt temperature of 78°C (which was the predicted optimal melt temperature for the GA+NN strategy for $T_{o\text{-}max}$). However, the ANN predictions do match the general shape of the ParaPower predictions, unlike the continued downward slope of the ParaPower profile, the ANN predicts a distinct minimum $T_{o\text{-}max}$ near a height of 100 μm and a width of 75 μm. This is why the GA reports an optimum width that is not at the upper bound. The relative flatness of the ParaPower results above a width of 60 μm shows that, despite this unphysical minimum, the impact on system performance is minimal.

IMPACT OF TRAINING DATA SET SIZE ON ANN-ASSISTED OPTIMIZATION

The results of an ANN-assisted optimization strategy depend heavily on the accuracy of the ANN when compared to the selected optimization algorithm and its set convergence criteria. The performance of an ANN can be impacted by the structure of the ANN (number of hidden layers, number of neurons per layer, activation function, training algorithm), the amount of training data and its subset distribution, and the randomly initialized weights.

Table 2 shows results while varying the size of the training data set for the optimization of $T_{o\text{-}max}$. Increasing the training data does not hurt the performance of an ANN, but there are diminishing returns with continuing to increase the training data, with the corresponding increases in computational time. Here, the benefit of increasing the training data stagnates past a data size of 250 cases, with the predicted $T_{o\text{-}max}$ for the optimized data set for this ANN and the ANN with 2380 cases being only within <1°C of each other. This shows that the parameters for the system optimum can be found within ~30 minutes, which is 13 times faster than the direct optimization coupled to ParaPower.

EMBEDDED COOLING: GRID-BASED GEOMETRY

To enable broader optimization of geometries beyond parallel channels with uniform heating, the viable PCM layer is discretized into a 10 x 10 grid of pockets that could be either PCM or Silicon (*Figure 1c*). The strategic placement of these pockets is optimized through the GA using a binary matrix: *1* denotes a PCM pocket and *0* denotes a silicon pocket. The GA has an optimization objective of minimizing $T_{o\text{-}max}$. We chose a metallic composite PCM with a melt temperature of 79°C; based on the results of the 2D parallel channel optimization.
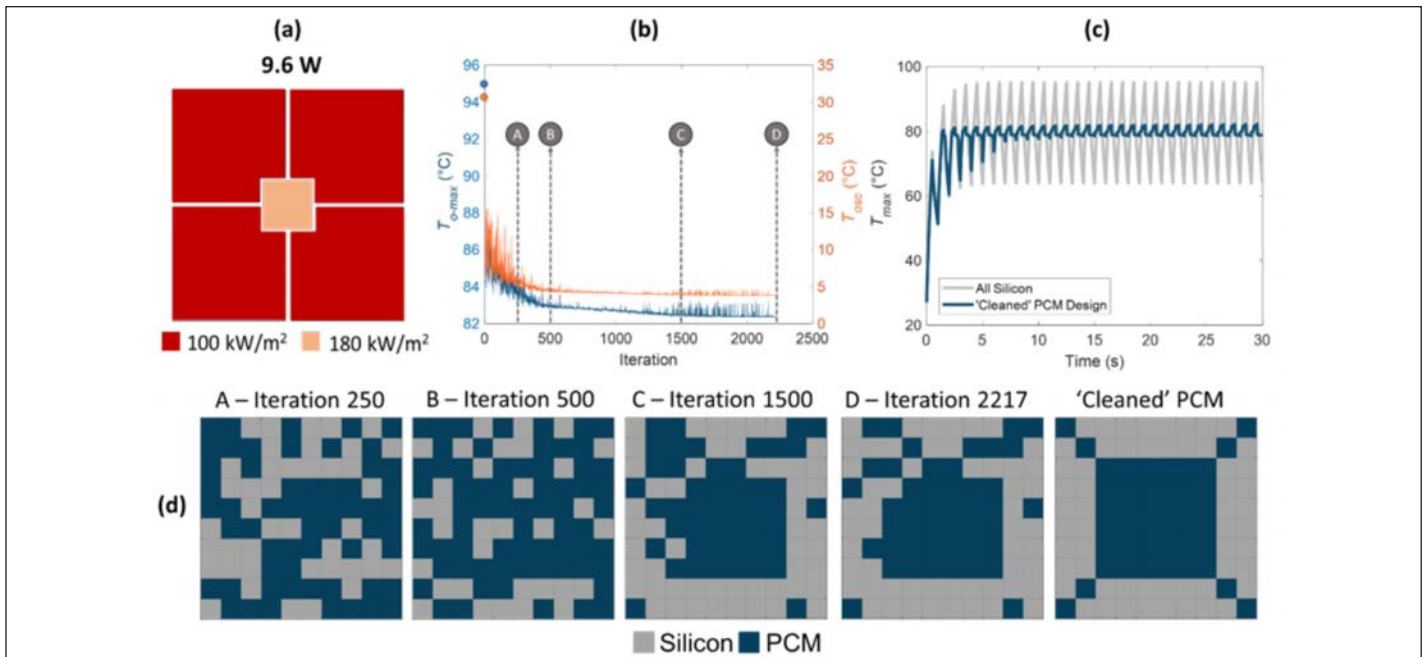
Figure 4: (a) Illustration of the powermap used for 3-D optimization (b) Performance of PCM embedded substrate as GA progress through 2217 iterations. (c) Thermal response of an unaltered all-silicon substrate compared to the optimized substrate. (d) PCM/silicon placements at various points in the GA Progression. The iteration locations are also noted in (b).

A power map (*Figure 4a*) is defined by first separating the heating layer into 4 large quadrants with a 2x2 cm hotspot zone in the center. The total chip dissipates 9.8 W. The GA optimization takes a total of 2217 iterations to optimize with a total computational time of 25 hours. *Figure 4b* shows the overall maximum temperature and amplitude of the temperature oscillations at each iteration of the optimization. *Figure 4c* shows the corresponding temperature evolution for the initial all-silicon starting point compared to the final design. An animation showing the evolution of the design and temperature metrics is available via bit.ly/MTEC_ML1, and for other heating patterns at bit.ly/MTEC_ML2 and bit.ly/MTEC_ML3.

The starting point (iteration 0) of the GA evolution graph (*Figure 4b*) shows the response for an all-silicon die. The reduction in T_{o-max} and T_{osc} after the very first iteration highlights the substantial improvement in system performance achieved with any addition of PCM. At iteration 250, there is no noticeable pattern in the PCM distribution: the PCM and silicon pockets are randomly distributed. At iteration 500, there are substantially more PCM pockets than silicon pockets. There is a visible pattern by iteration 1500, as the PCM is concentrated in the center as an 8x8 matrix with silicon pockets dominating the outer boundary of the viable PCM layer. The improvement in system performance now stagnates as the GA progress further. The final iterations resemble PCM lines radiating from the middle reservoir of PCM to the corners. A 'cleaning' operation is performed on the GA optimized pattern by leveraging symmetry and removing noticeable outliers such as 'islands' of PCM that are surrounded by silicon and vice versa. This 'cleaned' PCM design reduces T_{o-max} by 15% and has the added benefit of reducing T_{osc} by 80%.

CONCLUSIONS

To summarize, machine-learning based optimization with or without surrogate models improves the computational efficiency of the design process for embedded passive cooling layers. With the metallic PCM, adding PCM to the system significantly reduces both the maximum temperature and amplitude of temperature oscillations. These systems are of particular interest for passive cooling of mobile electronic devices and the embedded thermal capacitance can improve system performance. Beyond electronic devices, this same design strategy can be applied to other thermal management applications such as for batteries, automotive, and space applications.

REFERENCES

[1] ARL ParaPower, https://github.com/USArmyResearchLab/ParaPower
[2] L. Boteler, Multiple Domain Optimized Power Packaging, https://d2vrpothuwvesb.cloudfront.net/uploads/techops/fe1193cf-aa80-4708-b52a-762d2db1c00e/attachments/FY17-OCOH-ScMvr-33-Multiple-Dom_E7PFqYn.pdf
[3] IBM, What is Machine Learning? - https://www.ibm.com/cloud/learn/machine-learning
[4] Mathworks, How the genetic algorithm works. - https://www.mathworks.com/help/gads/how-the-genetic-algorithm-works.html
[5] Mathworks, What Is a Neural Network? - https://www.mathworks.com/discovery/neural-network.html
[6] Bhatasana and Marconnet, "Machine-learning assisted optimization strategies for phase change materials embedded within electronic packages", *Applied Thermal Engineering*, Accepted and In Press, 2021. https://doi.org/10.1016/j.applthermaleng.2021.117384

KEYNOTE SPEAKER
Andy Delano, Microsoft Corporation
Innovations in Thermal Management of Electronic Devices

Surmounting the challenges and limitations encountered in any endeavor requires innovation. Not only do we have to discover how to see past our own limitations, we also have to convince our colleagues for the need to change and follow through with the necessary leadership. This talk is an inspiring tour of innovations in thermal engineering.

SHORT COURSES
MONDAY MARCH 21, 2022

Short Course 1: 8AM-10:15AM *The Role of Intellectual Property in Protecting Semiconductor Innovation* Instructors: Neil A. Steinberg and Dinesh N. Melwani	**Short Course 3: 8AM-12:15PM** *Thermal Comfort Considerations for Electronics Cooling and Design* Instructors: Dr. Mark Hepokoski and Craig Makens
Short Course 2a: 10:15AM-12:15PM *Fundamentals of Acoustics* Instructor: David Nelson	
Short Course 2b: 1:30PM-3:30PM *Fundamentals of Noise Control* Instructor: David Nelson	**Short Course 4: 1:30PM-5:30PM** *Photonic and Metamaterial Control of Radiative Heat Transfer* Instructor: Aaswath P. Raman
Short Course 2c: 3:30PM-5:30PM *Example Noise Control Applications* Instructor: David Nelson	

SPONSORS

celsia°

SIEMENS

CoolIT systems

TECHNICAL SESSIONS
MARCH 22-24, 2022

Liquid Cooling

Suchismita Sarangi, Intel Corporation
Single-Phase Immersion Cooling Performance in Intel Servers with Immersion Influenced Heatsink Design

Ty Kieger, San José State University
Computational Analysis of Changing Wavelength and Amplitude Effect on Bottom Rib and Side Rib Wavy Microchannel Heat Sinks

Dinumol Varghese, United Arab Emirates University
Parametric Study of Fluid Flow and Heat Transfer in Microchannel Heatsink Embedded with Semi-circular Cavities for Thermal Management of Microelectronics Chips

Consumer Products

Robin Bornoff, Siemens Digital Industries Software
Application of JESD51-14 to BGA Package Styles

Burhan Ozmat, OZER Advanced Technologies
PCM Infiltrated Metal Foam Based Advanced Passive Heat Exchangers

Vibin Shalom Simon, The University of Texas at Arlington
Characterization of Parallel and Opposed Control Dampers to Observe the Effect on Thermal Mixing of Air Streams in an Air-Cooling Unit

Two-Phase Cooling

Sang Muk Kwark, Laird Thermal Systems
Evaluation of Cooling Capacity of Refrigeration System with Limited Charge of R-290

Lieven Vervecken, Diabatix
Generative Design and Experimental Validation of a Two-phase Heat Sink

Najmeh Fallahtafti, Binghamton University
Comparison of Two Designs of an Impingement Two-phase Cooling Cold Plate Intended for High Heat Flux in Data Center

Thermal Interface Materials

Xuefeng Lin, Laird Thermal Systems
Optimized Dispensing of Thermal Interface Materials: Issues and Progress

Claire K Wemp, DuPont
Measuring Change in Thermal Performance of Multi-layer Laminates after Reliability Testing

Andras Vass-Varnai, Siemens Digital Industries Software
Characterization of Thermal Interface Materials for Power Electronics Applications

Lyndsey Scammell, BNNT Materials LLC
Boron Nitride Nanotubes for Advanced Thermal Management

Data Centers

Javier Avalos Garcia, Intel Corporation
Intel Air Cooling Server Conversion to Two Phase Immersion Cooling and Thermal Performance Results

Eric D. McAfee, Intel Corporation
Subzero System Heating for Outdoor Applications

Emerging Technologies

Vito Di Pietro, TWI Ltd.
Manufacturing of Integrated Thermal Management Solutions Using Friction Stir Channelling Derived Process CoreFlow™

Ross Wilcoxon, Collins Aerospace
Oscillating Heat Pipe Thermal Performance and Stability Limits

Azita Soleymani, Electronic Cooling Solutions
Thermal and Hydraulic Characterization of a Double-sided Cold Plate Used in AI Systems

Jungho Lee, Ajou University
Thermal Management Device with Boiling-driven Heat Spreader

Heat Transfer and Pressure Drop Correlations for Manifold Microchannel Heat Sinks

Sevket U. Yuruker, Raphael K. Mandel, Amir Shooshtari and Michael M. Ohadi
Department of Mechanical Engineering, University of Maryland,
College Park, MD, USA, 20740
Email: ohadi@umd.edu

Sevket Umut Yuruker

Sevket is a senior mechanical engineer at Tesla. He received his BS in mechanical engineering from Ozyegin University, Turkey. After graduating in 2015, he joined the University of Maryland as a graduate research assistant to pursue a MS degree in mechanical engineering, with his thesis focusing on thermoelectric cooling of high heat flux electronics. After graduating in 2017, he worked as a thermal engineer in Baykar Technologies, a private aerospace company in Turkey, where he was the thermal lead on multiple projects related to thermal management of avionic components in MALE class UAVs. In August 2018, he started his PhD studies at the University of Maryland, in the AHX-PI (formerly known as S2TS) group. His PhD research was on thermal management of power electronics, with extensive utilization of single-phase manifold microchannel cooling, additive manufacturing, and development of physics based closed form correlations for manifold microchannel systems. After graduating in 2021, he joined Tesla's power electronics team and currently works on packaging and thermal management of next generation power conversion systems of electric vehicles.

Raphael Mandel

Raphael is an Assistant Research Scientist in the Smart and Small Thermal Systems Laboratory at the University of Maryland, College Park. There, he serves as technical lead on numerous projects involving single-phase and two-phase thermal management, thermodynamics, topological and multi-physics co-design and optimization, and additive manufacturing. He received his Ph.D. in Mechanical Engineering in 2016 from the University of Maryland, College Park, where he designed a novel "FEEDS" cooler capable of dissipating heat fluxes in excess of 1 kW/cm2 at vapor qualities exceeding 85%. He has published more than 25 peer-reviewed technical publications in the fields of fluid dynamics and heat transfer.

Amir H. Shooshtari

Amir is a Research Associate Professor in the Small and Smart Thermal Systems Laboratory at the University of Maryland, College Park. He received his Ph.D. in 2004 in mechanical engineering. Since 2005 he has been a member of the research faculty at the University of Maryland. His areas of research include additive manufacturing, design optimization, computational fluid dynamics, thermal management of electronics, and process intensification. Dr. Shooshtari is the author or co-author of more than 70 publications in international journals and conferences. He is a member of ASHRAE and ASME.

Michael Ohadi

Michael is a Minta Martin Professor of Mechanical Engineering at the University of Maryland, College Park. Ohadi's research has focused on heat transfer enhancement of single phase and two-phase flows through process intensification utilizing multi-scale design optimization, materials, and manufacturing techniques. From 2016 to 2020, Ohadi served as Program Director (PD) at the U.S. department of energy, Advanced Research Project Agency-energy (ARPAE), where he led the development of programs in thermal management and energy conversion systems. Ohadi received his Ph.D. in mechanical engineering from the University of Minnesota and joined the University of Maryland in 1990. He is a fellow member with both ASME and ASHRAE and has published more than 300 peer reviewed technical publications in his fields of expertise.

NOMENCLATURE

A	area, m^2
AR	aspect ratio
Cp	specific heat, J/kg-K
fRe	Poiseuille number
IR	inlet ratio
k	thermal conductivity, W/m-K
L	length, m
h	height, m
Nu	Nusselt number
P	perimeter, m
Re	Reynolds number
w	width, m
v	velocity, m/s
T	temperature, °C
ΔT	temperature difference, °C

ΔP	pressure drop, Pa
Q	heat, W
D_h	hydraulic diameter, m
h	heat transfer coefficient, W/m^2-K

Greek symbols

ρ	mass density (kg/m^3)
μ	viscosity (N-s/m^2)
ε	effectiveness

Subscripts

in	inlet
out	outlet
ch	channel
f	fluid
man	manifold
mc	microchannel
max	maximum

INTRODUCTION

Conventional microchannel cooling has been proven capable of removing high heat fluxes, but usually at significant pressure drops. On the other hand, manifold microchannel systems offer high heat transfer coefficients/heat removal rates, but at significantly reduced pressure drops compared to traditional microchannel cooling [1–5]. Manifold-microchannels (MMC) can achieve reduced pressure drops at increased heat transfer rates by dividing long microgrooves into an array of parallel microchannels using manifolds, as shown in *Figure 1*. However, the optimal design of a manifold microchannel system depends on the particular application and its operating conditions.

Since currently validated correlations do not exist for manifold microchannels, optimization is usually performed using CFD, which is computationally demanding and time-consuming. Instead, the pressure drop and heat transfer of a given manifold-microchannel design, for specific fluid and operating conditions, often can be easily calculated if the two most relevant dimensionless parameters, Nusselt and Poiseuille numbers, are known a priori. This would reduce the engineering efforts and computational cost to design effective MMC systems to be utilized in a variety of electronic cooling applications with ultra-high heat fluxes, such as power electronics systems, high power laser systems, electric motor cooling and data center thermal management.

In this study, a wide range of dimensionless parameters that define the manifold microchannel design and its operating conditions were simulated using a commercial CFD software package to obtain pressure drop and heat transfer coefficients. Their corresponding dimensionless performance parameters, namely the Nusselt and Poiseuille numbers, are then curve fitted into a correlation, details of which, including an optimization case study at the end, have been previously published by Yuruker et al. [6]. Finally, a step-by-step procedure of how the correlation can be utilized in predicting the performance of a real heatsink design is provided with an example case.

ANALYSIS
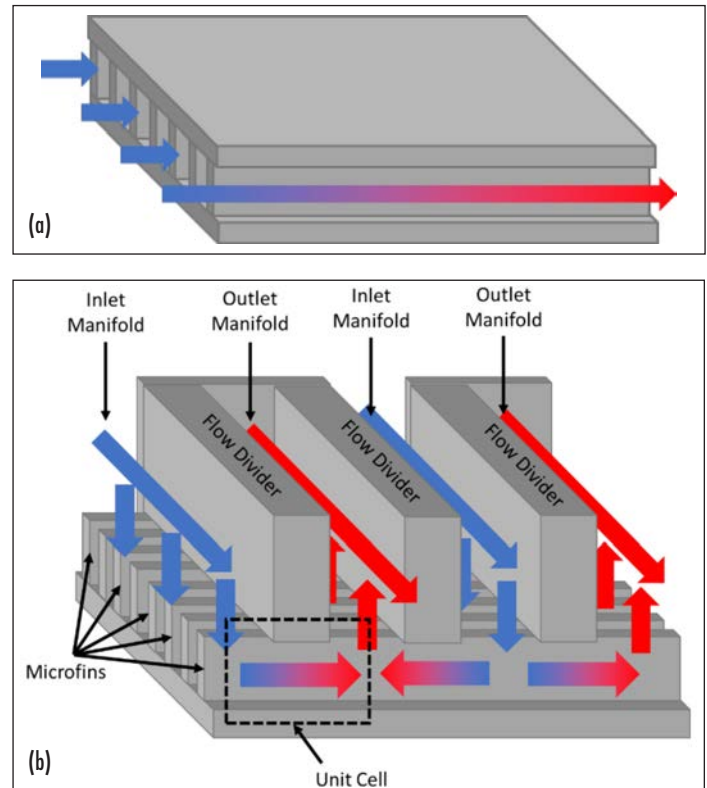
Figure 1: a) Traditional/straight microchannel system b) Manifold microchannel system.

Due to the periodic nature of manifold-microchannels, the computational domain chosen for this study is a unit cell portion of the complete manifold microchannel system, shown by dotted lines in *Figure 1*. The unit cell with relevant dimensions and boundary conditions is shown in *Figure 2*. Symmetry boundary conditions are imposed on the transparent sides of the channel while a wall boundary condition is applied on the remaining sides. A constant temperature is maintained on the bottom wall and fin wall, while the top wall is adiabatic due to the assumption that the manifold is pressed

onto the manifold and that the manifold is not a thermally conductive material (such as plastics); for cases where the manifold is metal (or thermally conductive) and is in good thermal contact with microchannels, a separate set of simulations would need to be performed. Constant velocity and temperature conditions are applied at the inlet, and zero pressure is applied to the pressure outlet. For simplicity, the inlet and outlet lengths are always equal in this study and the definitions of the geometric variables are shown in *Figure 2*.

The assumptions and simplifications used in the CFD model are listed as follows:

(1) Steady-state, laminar and incompressible flow
(2) Effect of gravity is negligible
(3) Constant fluid properties
(4) Constant wall temperature
(5) Contraction/expansion at the manifold-microchannel interface have negligible effect on heat transfer and pressure drop inside the microchannel.
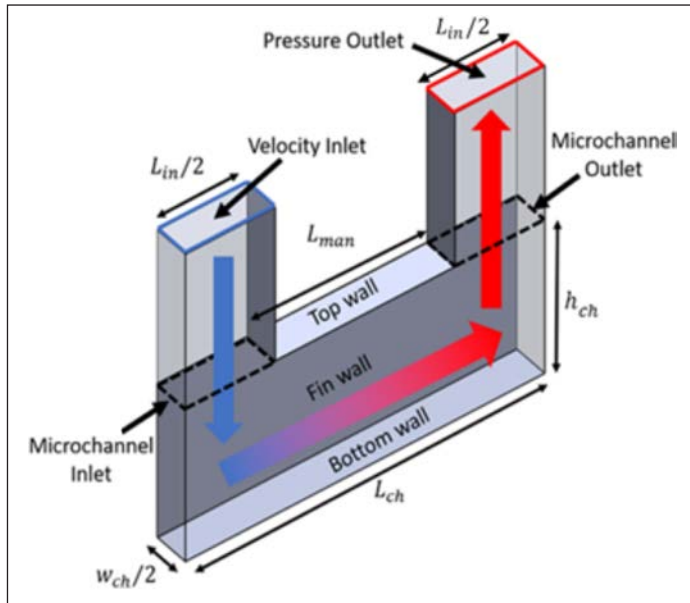

Figure 2: Unit cell manifold microchannel model.

The total pressure drop across the MMC system will include contribution from the manifold section as well, but as mentioned above this is not in the scope of this work. For this, external calculations or CFD will be required. One suggestion is utilization of a hybrid method introduced by Arie et.al., which assumes a 1D flow in the manifold, enabling reduction of the governing equations into a single differential equation as a function of velocity in the manifold [9,10]. Another suggestion is building a system level CFD model of the MMC architecture, yet representing the microchannel array as a unified porous media domain [11]. The velocity vs. pressure drop and heat transfer characterization of the microchannel can be priorly done using the correlation given in this study, and applied to the porous media settings. This method significantly reduces the mesh complexity and computational power requirement as small microchannels do not need to be modeled individually.

A useful correlation should be applicable to a wide range of geometries and operational conditions. To make this possible, the manifold-microchannel geometry is defined in terms of three dimensionless parameters: aspect ratio (AR), inlet ratio (IR), and velocity ratio (VR), which are defined in *Eqs. (1)-(3)*:

$$AR = \frac{h_{ch}}{w_{ch}} \tag{1}$$

$$IR = \frac{L_{in}}{L_{ch}} \tag{2}$$

$$VR = \frac{V_{in}}{V_{ch}} = \frac{2h_{ch}}{L_{in}} \tag{3}$$

where w_{ch}, h_f, L_{in}, and L_{ch} are defined in *Figure 2*.

The Reynolds number in the microchannel is the first operational dimensionless parameter to be determined and is defined as

$$Re = \frac{\rho V_{ch} D_h}{\mu} \tag{5}$$

where D_h is the hydraulic diameter and is defined as

$$D_h = \frac{4A}{P} = \frac{2w_{ch}h_{ch}}{w_{ch} + h_{ch}} \tag{6}$$

The second operational dimensionless parameter considered is the Prandtl number, which is the main input related to fluid selection in the numerical analysis:

$$Pr = \frac{C_p\mu}{k_f} \tag{7}$$

Once these five parameters are specified -*AR, IR, VR, Re,* and *Pr* - the microchannel geometry and operational conditions for the CFD simulation can be computed from *Equations 1-7*.

Since the main points of interest are the pressure drop and heat transfer within the microchannel itself, the contribution from the manifold portion of the model is excluded by measuring pressures and temperatures at the microchannel inlet and microchannel outlet surfaces, as shown in *Figure 2*. The pressure drop is non-dimensionalized as the Poiseuille number, *fRe*, and is defined as

$$fRe = \frac{2\Delta P D_h{}^2}{\mu V_{ch} L_{ch}} \tag{8}$$

with

$$\Delta P = \bar{P}_{mc,inlet} - \bar{P}_{mc,outlet} \tag{9}$$

where P, $\bar{P}_{mc,inlet}$ and $\bar{P}_{mc,outlet}$ are the area-averaged pressures computed directly by the CFD software on the microchannel inlet and outlet faces, respectively (see *Figure 2*):

Similarly, the Nusselt number, *Nu*, is used as the dimensionless performance metric for heat transfer. The Nusselt number is calculated as

$$Nu = h_{wall} * D_h/k_f \qquad (10)$$

where h_{wall} is the heat transfer coefficient at the walls and k_f is the thermal conductivity of the fluid. The heat transfer coefficient can be calculated from the number of transfer units, NTU, and

$$h_{wall} = \frac{\dot{m}C_p}{A_{wall}}NTU \qquad (11)$$

For a constant temperature condition, NTU is related to the heat exchanger effectiveness, ε, as

$$NTU = -\ln(1 - \varepsilon) \qquad (12)$$

and ε is the ratio of actual heat transfer at the walls to the maximum possible heat transfer:

$$\varepsilon = \frac{Q}{Q_{max}} = \frac{T_{out} - T_{in}}{T_{wall} - T_{in}} \qquad (13)$$

where T_{in} and T_{out} are the mass-averaged fluid temperatures at the microchannel inlet and outlet, respectively and are computed directly with CFD. Using *Equations 8-13*, the two dimensionless performance metrics *fRe* and Nu are calculated from the dimensional results obtained by CFD.

To accurately capture the boundary layer near the walls with the least computational expense, mesh inflation was used on all walls and in all three dimensions. To ensure that the simulations were mesh-independent, each simulation was performed with a series of mesh levels with the number of cells ranging roughly from 40,000 to 160,000. Only cases with less than 1% difference between the two finest mesh levels were considered mesh-independent and the rest were discarded. The simulations are solved with a first-order upwind scheme using the coupled algorithm in the CFD software. The convergence criteria for the momentum/continuity and energy are set to 1×10^{-5} and 1×10^{-12}, respectively.

RESULTS

Table 1: Range of dimensionless design parameters	
Dimensionless Design Parameters	**Range**
AR	10
IR	0.05, 0.1, 0.2, 0.4, 0.6, 0.8
VR	1
Re	10, 20, 50, 100, 200, 500, 1000
Pr	0.5, 0.7, 1, 2, 5, 7.5, 10, 20, 50, 100

The range of dimensionless variables considered in this study, given in *Table 1*, corresponds to 490 unique simulations. To limit the size of this study, only one value of AR and VR is considered. The Reynolds number was varied from 10 to 1000 to encompass a wide range of flow conditions from fully-developed laminar to

developing laminar flow while avoiding transition to turbulent flow. Similarly, Prandtl number was varied from 0.5 to 100 to encompass most fluids, such as gasses, dielectric liquids, and oils.
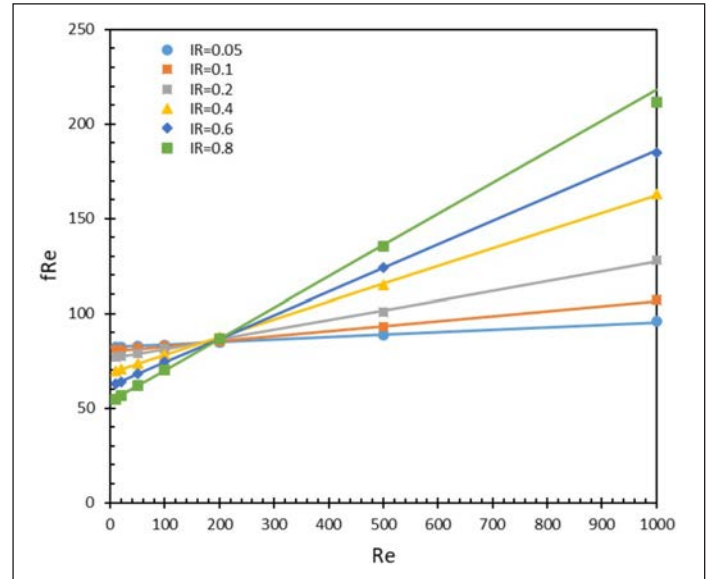

Figure 3: Poiseuille number as a function of Reynolds number. Symbols represent the CFD data and lines represent the curve fitted data.

The 490 simulations were performed, as described, and the resultant performance metrics - Poiseuille and Nusselt numbers - were found to be functions of the three dimensionless parameters, IR, Re, and Pr. A linear relationship between Poiseuille number and Reynolds number was observed for all IR values, as shown in *Figure 3*. Thus, it can be concluded that fRe has the form

$$fRe = a \times Re + b \qquad (14)$$

where *a* and *b* coefficients solely depend on the geometric parameters AR, IR, and VR. The constant term b represents the contribution from fully developed flow, and is independent of Re, as expected. However, the channel has a developing region, as well as two turns at the inlet corner and outlet corner, which contribute to fRe and their magnitude scales with Re. Thus, the first term in *Equation 14 a $\times$ Re*, corresponds to the contribution from turning and developing flow losses. At smaller IR, developing and turning losses are smaller, as the channel is very long and the majority of the pressure drop occurs in the straight section of the channel. For high IR, the straight section is short and the majority of the losses are due to turning and developing flow and the flow may never fully develop. For lower Reynolds, the developing and turning loss contributions are small (as they directly scale with Re) and thus it can be seen that low IR cases (with longer straight channel sections) have larger fRe. Similarly, for larger Reynolds numbers, the turning and developing losses dominate; therefore those cases with larger IR (with shorter straight sections, almost like a U-shape) have larger fRe. Interestingly at Re=200, there seems to be a balance between the turning/developing/ developed flow contributions to fRe, and it collapses to a single point. Thus, for the chosen AR and VR, at Re=200 the fRe is not a function of

IR. It must be noted that the Reynolds at which this happens is a function of AR and VR and will not always occur at 200 for other values of AR and VR. Since only IR was varied in the present work, only the variation of *a* and *b* as a function of IR is discussed. The variation of *a* and *b* with IR is shown in *Figure 4*.
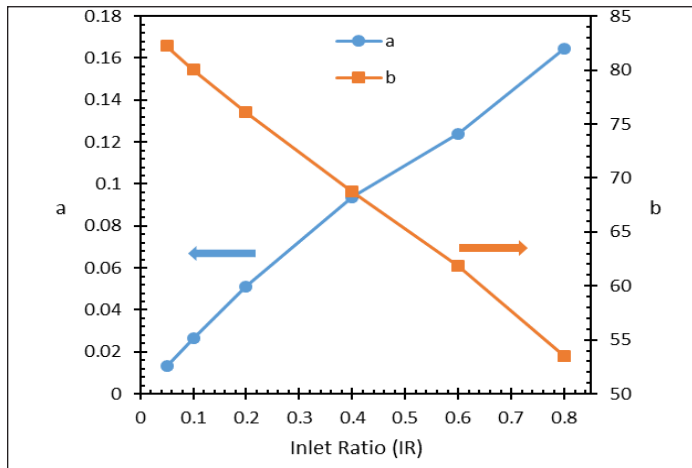

Figure 4: Curve fitted coefficients of fRe.

The results indicate that the multiplier coefficient *a* increases with Re while *b* decreases. *a* and *b* seem to have a very linear behavior and can be fitted linearly with IR for ease of use for the readers, however it must be noted that for IR>0.8 or for other values of AR or VR, the coefficients may not always behave linearly, and thus a linear fit may be a large source of error.

As IR approaches 0, the geometry approaches that of a straight microchannel. According to the literature, for a fully developed rectangular duct with AR=10, fRe is ~84 [7]. Thus, a noteworthy observation is that the curve fitted coefficient b also approaches this value as IR → 0, which can be visually seen in *Figure 4*.
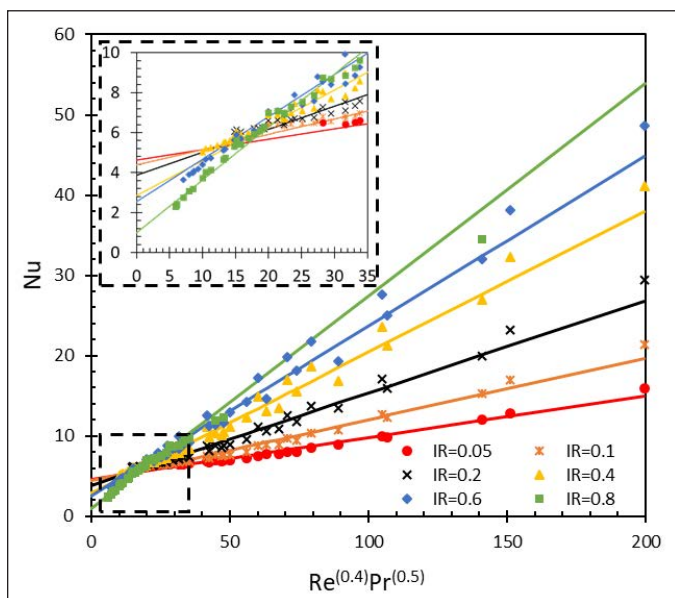

Figure 5: Nusselt number as a function of $Re^{(0.4)}Pr^{(0.5)}$. Markers represent the CFD data and lines represent the curve fitted data.

Similarly, it was observed from the data shown in *Figure 5* that the Nusselt number has a linear relationship with $Re^{0.4}Pr^{0.5}$. The form of the Nusselt number is similar to the form of the well-known Dittus-Boelter and Sieder-Tate equations [8]. However, in both Dittus-Boelter and Sieder-Tate correlations, the condition where Re approaches zero is not well accounted for, since the correlation is only valid for turbulent flows. For laminar flows, it is known that even if Re=0, fully developed heat transfer will occur and thus, the Nusselt number will be nonzero. Thus, an additional term 'n' is added to the Dittus-Boelter equation to establish an expression that is valid in the laminar flow regime:

$$Nu = k \times Re^{0.4}Pr^{0.5} + n \qquad (15)$$

The variations of *k* and *n* with IR are shown in *Figure 6*.
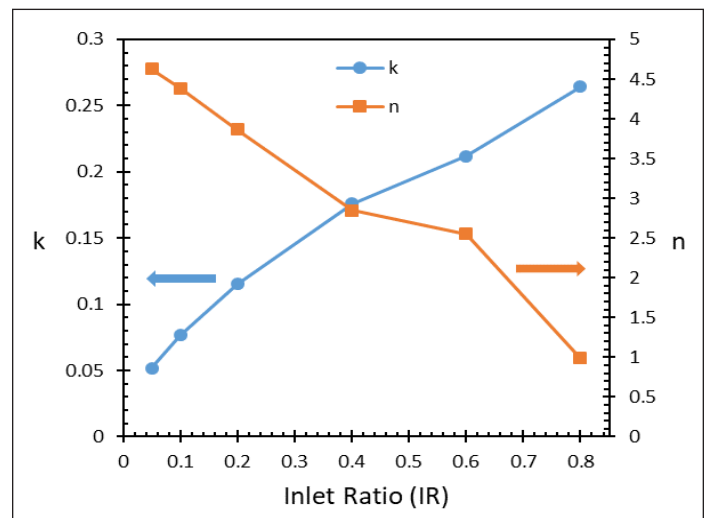

Figure 6: Curve fitted coefficients of Nu.

When the correlation was tested against the data points used in its creation, a mean error (deviation) of 0.4% and maximum error of 0.7% for fRe were observed, respectively. For Nu, the mean error was again 0.4%, while the maximum error was within 11.2%, which is reasonably accurate.

A STEP-BY-STEP GUIDE FOR USING THE CORRELATION

An example heatsink design and its thermo-fluidic performance evaluation are given below to serve as a guide in using the correlation. A MMC heatsink with a channel width of 0.1mm, channel height of 1mm, channel length of 5mm, and the inlet length of 2mm is considered. In this design, there will be 4 channels in the direction of the channel length and 20 channels in the direction of its width, resulting in a total of 80 microchannel segments, such as that shown in *Figure 2*. When *Equations 1-3* are evaluated for the unit cell geometry, the dimensionless variables are AR=10, VR=1, and IR=0.4. If the working fluid is water at room temperature (Pr=7, μ=0.01 Pa-s, ρ=1000kg/m³, k_f=0.6 W/mK), and if the total volumetric flow rate into the MMC heatsink is 1.1e-5 m³/s, each channel gets 1/80th of this flow rate, i.e., 1.38e-7 m³/s. For this flow rate, the Reynolds number inside a channel can readily be calculated using *Equations 5-6* to be Re=250.

To predict the pressure drop for the given geometry and operating conditions, *Eq.13* has to be evaluated. The terms "a" and "b" for IR=0.4 can be found in Figure 4 to be 0.09 and 69 respectively. Then, using *Equation 13* at Re=250 we calculate fRe=91.5. Now using *Equation 8*, pressure drop (ΔP) can be readily calculated to be 104 Pa.

Similarly, to predict the heat transfer coefficient for this design, *Equation 15* must be evaluated at the given Re=250 and Pr=7.5 conditions. The coefficients "k" and "n" for IR=0.4 can be found from *Figure 6*, and are 0.17 and 2.9, respectively. Now using *Eq 15*, we find Nu=7.14. Using *Equation 10*, h_{wall} can be readily calculated to be 23,555 W/m²K. If an effective base heat transfer coefficient for the entire heatsink is desired to be calculated, the fin efficiency equation, which is commonly found in any heat transfer book, can be utilized for the selected solid material conductivity and fin thickness [6]

This entire process can be programmed into commercially available coding software and any particular design at any operational conditions (flow rate and fluid selection) can be evaluated nearly instantly. This enables many design iterations to be evaluated in a significantly reduced time as opposed to CFD analyses. Therefore, it is a powerful tool when a design optimization is to be performed. Detailed examples of such an optimization process, with corresponding CFD validations, can be found in [6]

CONCLUSIONS

This work presented a convenient method for researchers and engineers to evaluate heat transfer and pressure drop performance of manifold microchannel heat sinks using a closed-form correlation. The correlation circumvents the need for computationally intensive CFD analysis and provides reasonably accurate results with maximum errors within 1% for pressure drop, and 12% for heat transfer predictions. The computational time required for optimizing the design of a manifold microchannel system is reduced from weeks to seconds. This enables and encourages MMC systems to be adopted and utilized in high heat dissipating electronic systems, such as high-power laser systems, power converter/inverter systems, electric motors applications as well as data center thermal management.

For future work, the range of the correlation should be widened to cover all possible geometrical parameters AR, IR, and VR, thus allowing diverse microchannel designs across different application areas to be evaluated.

REFERENCES

[1] G. M. Harpole and J. E. Eninger, "Micro-channel heat exchanger optimization," in *Proceedings - IEEE Semiconductor Thermal and Temperature Measurement Symposium*, Feb. 1991, pp. 59–63, doi: 10.1109/stherm.1991.152913.

[2] D. Copeland, M. Behnia, and W. Nakayama, "Manifold microchannel heat sinks: Isothermal analysis," *IEEE Trans. Components Packag. Manuf. Technol. Part A*, vol. 20, no. 2, pp. 96–102, Jun. 1997, doi: 10.1109/95.588554.

[3] E. Cetegen, "FORCE FED MICROCHANNEL HIGH HEAT FLUX COOLING UTILIZING MICROGROOVED SURFACES," University of Maryland, College Park, 2010.

[4] R. Mandel, A. Shooshtari, and M. Ohadi, "A '2.5-D' modeling approach for single-phase flow and heat transfer in manifold microchannels," *Int. J. Heat Mass Transf.*, vol. 126, pp. 317–330, Nov. 2018, doi: 10.1016/j.ijheatmasstransfer.2018.04.145.

[5] S. U. Yuruker, R. K. Mandel, P. McCluskey, and M. Ohadi, "A Vertically-Enhanced Manifold Microchannel System (VEMMS) for Thermal Management of Power Electronics," *IEEE Trans. Components, Packag. Manuf. Technol.*, pp. 1–1, 2021, doi: 10.1109/TCPMT.2021.3082771.

[6] S. U. Yuruker, R. K. Mandel, A. Shooshtari, and M. M. Ohadi, "A metamodeling approach for optimization of manifold microchannel systems for high heat flux cooling applications," in *InterSociety Conference on Thermal and Thermomechanical Phenomena in Electronic Systems, ITHERM*, 2019, vol. 2019-May, doi: 10.1109/ITHERM.2019.8757232.

[7] S. I. Edition, Y. a Çengel, and J. M. Cimbala, "Fluid Mechanics : Fundamentals and Applications," pp. 1–117, 2010, doi: 10.1016/B978-0-12-405935-1.18001-3.

[8] Y. A. Çengel and A. J. (Afshin J. Ghajar, *Heat and mass transfer : fundamentals & applications*. .

[9] Arie, M. A., Shooshtari, A. H., Dessiatoun, S. V., Al-Hajri, E., & Ohadi, M. M. (2015). Numerical modeling and thermal optimization of a single-phase flow manifold-microchannel plate heat exchanger. International Journal of Heat and Mass Transfer, 81, 478-489.

[10] Arie, M. A., Shooshtari, A. H., Rao, V. V., Dessiatoun, S. V., and Ohadi, M. M. (December 28, 2016). "Air-Side Heat Transfer Enhancement Utilizing Design Optimization and an Additive Manufacturing Technique." ASME. J. Heat Transfer. March 2017; 139(3): 031901. https://doi.org/10.1115/1.4035068

[11] Battaglia, F, Mandel, R, Shooshtari, A, & Ohadi, MM. "A Porous Medium Approach for Single-Phase Flow and Heat Transfer Modeling in Manifold Microchannel Heat Exchangers." *Proceedings of the ASME 2020 International Technical Conference and Exhibition on Packaging and Integration of Electronic and Photonic Microsystems*. Virtual, Online. October 27–29, 2020. V001T05A002. ASME. https://doi.org/10.1115/IPACK2020-2564

Thermal Comfort Considerations for Electronics Cooling and Design

Mark Hepokoski and Alex Ockfen
ThermoAnalytics
Meta Reality Labs

INTRODUCTION

ASHRAE defines thermal comfort as "that condition of mind that expresses satisfaction with the thermal environment" [1]. While engineers and designers are typically familiar with the thermal safety and compliance standards required in their industry [2], thermal comfort is less well understood and often treated as an afterthought in the design process. However, thermal comfort should be considered early in any product development process. Not only are thermal comfort thresholds lower than their safety counterparts, but thermal comfort-related misses can hinder the success of a design due to factors such as poor product reviews.

As illustrated in *Figure 1*, the human body is often cooler than commercial electronic items, such as laptops or mobile phones. If the heat flux resulting from immediate and/or prolonged contact with an electronic device negatively impacts comfort, satisfaction with the product will consequently also be negatively affected. In light of this, comfort in the consumer electronics industry is expected to become increasingly important as people become more directly coupled with their electronics devices.

This primarily is being observed in the wearables industry with devices such as smartwatches, virtual reality, and augmented reality products.

Figure 1: Infrared image of common consumer electronics during outdoor usage (°C)

Mark Hepokoski
Mark is the Chief Scientist and Chief Technology Officer (CTO) at ThermoAnalytics, where he leads the research and development of simulation and testing methods for the TAITherm family of commercial heat transfer CAE tools. During his past tenure as a Principal Investigator of human thermo-physiology and thermal comfort projects, he has accumulated almost two decades of experience developing a complex thermal model of the human body that is widely used in the automotive industry for developing comfort-focused climate control technology. Dr. Hepokoski received his B.S. in Engineering Science and Mechanics from Virginia Tech. He also holds an M.S. degree in Mechanical Engineering and a Ph.D. in Mechanical Engineering-Engineering Mechanics from Michigan Technological University.

Alex Ockfen
Alex is simulation engineer at Meta (formerly Facebook), providing technical leadership for thermal and structural design of consumer electronics products. He held previous positions at Raytheon where he obtained experience in thermal management and electronics cooling of a wide range of aerospace and defense applications. He has more than 10 journal and conference publications, is an inventor on multiple patents, is a professional mechanical engineer, and is currently serving as vice program chair of the SEMI-THERM conference.

Thermal comfort is a complex phenomenon that depends on factors including personal preference, local environment, geographical location, product use case, product type, user interface, geometry, and material to name a few. The wide range of contributing factors results in a large variation in thermal comfort metrics and indicators, including temperature, heat flux, and skin wetteness. *Table 1* provides a non-exhaustive snapshot of various comfort limits identified in the literature. It is also possible that there are interactions between multiple metrics, such as temperature and skin wetteness.

Table 1: Examples of Thermal Limits for Comfort and Safety			
Thermal Limits	**Limit Type**	**Value**	**Ref.**
Safety	Touch Temperature (> 8hr)	43°C	[2]
	Touch Temperature (> 1min)	48°C	
Comfort	Touch Temperature*	40-48°C	[3]
		41°C	[4]
		44°C	[5]
		45°C	[6]
	Heat Flux	400 W/m^2	[4]
	Skin Wetteness	0.30-0.36	[7]
* Touch temperature limits typically correspond to the initial onset of pain/discomfort, not the first thermal sensation			

Given both the importance and complex nature of thermal comfort in electronics design, a logical process is needed to design for thermal comfort. Successful design typically combines user testing and comfort modeling to enable data-driven design decisions. *Figure 2* illustrates one embodiment of a notional process for integrating thermal comfort into the design cycle.
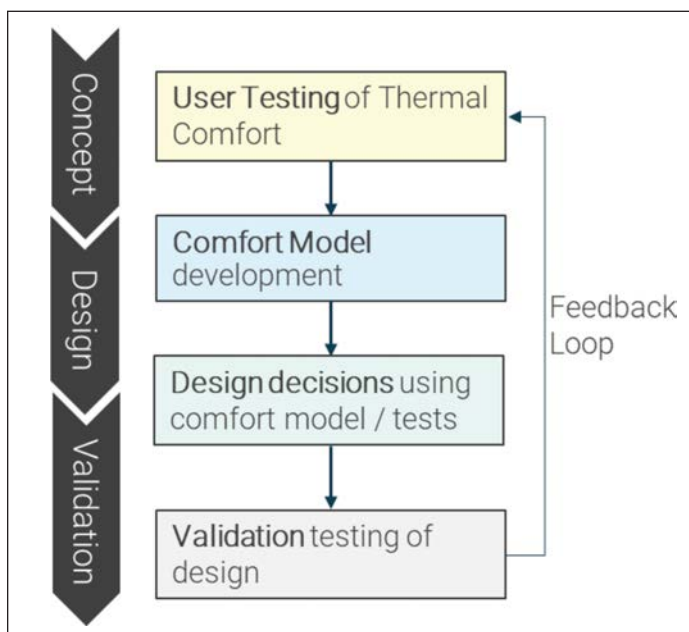

Figure 2: Integrating thermal comfort into the design process

USER TESTING

Thermal sensation is affected by warm and cold subcutaneous thermo-receptor discharge rates, which, in turn, are correlated with human body temperature [8]. Understanding how hot or cold stimuli may be perceived by a human subject requires a comprehensive assessment of the heat generated and distributed within a human body and the heat transfer between the body and its environment. Thermal perception can be described in terms of thermal sensation (how hot or cold one feels) and/or thermal comfort (whether or not the sensation feels good or bad) [9][10].

In addition to thermo-receptors, "touch" receptors may also be important in thermal perception studies. For example, cool air impinging on human skin can cause so-called draft discomfort, which correlates to the response of both mechanoreceptors and thermo-receptors when stimulated in tandem [11]. For example, draft discomfort is a significant concern in the design of architectural and automotive environments since climate control systems typically rely on air movement to modulate the ambient temperature. Similarly, the combination of these same receptor responses, when processed in the brain, elicits the perception of wetness. This may cause discomfort during an exposure in which sweat is produced and leads to an uncomfortable feeling of stickiness after the sweat has dried [12]. Wetness and stickiness should be considered in thermal perception studies involving warm to hot environments and/or work-rest cycles incorporating high activity.

While there is a clear correlation between thermo-physiological state and thermal perception within an average population sub-group, there will always be variability among individuals [13]. While a portion of this variability can be attributed to differences in individual subjective thermal preferences, other, more objective factors that influence thermo-physiological state, can be controlled to some extent. If one of the objectives of a test is to reduce variability, it is important to define a test protocol that ensures all participants are outfitted in a standardized clothing ensemble (e.g., jeans and t-shirt) and perform the same activity (e.g. a prescribed work-rest cycle). The initial thermo-physiological state can strongly impact test results [14]. This influence can be mitigated by ensuring that test participants control their activity prior to testing by, for example, requiring that they refrain from vigorous exercise a sufficient number of hours before the testing. Some aspects may be more challenging to control, but can nevertheless be addressed by using a larger study population so that test data can be segregated and analyzed *a postiori* according to subgroups of individuals that share the same personal characteristics, such as ethnicity, sex, levels of acclimatization, and physical fitness.

Subjective responses can be gathered by a variety of means, including by the use of paper or electronic forms filled out by test participants throughout the exposure [15]. Participants can also be prompted intermittently to provide a verbal description of their thermal state [16]. While such an approach can be labor-intensive,

it does provide a more natural experience for the test participant and can improve reliability and consistency in test results.

For most applications, overall thermal comfort is the primary metric that ultimately needs to be gathered from a test. However, for a deeper understanding of how the participant's thermophysiological state may be influencing comfort, it can be valuable to also obtain a measure of the participant's overall thermal sensation. Additionally, since overall comfort correlates well with the comfort of the two most uncomfortable body segments, it can be informative to have test participants identify these along with the local sensation and comfort of these segments. It is critical that wetness perception and air movement/draft perception are measured if sweating or air movement are likely to occur during the exposure.

The psychology of an individual can also bias results. Studies have shown that thermal perception can be influenced by the color of a room or whether one has control over the environment. To mitigate such influences, the test should be designed to obfuscate the experimental setup details or its history and reduce bias derived from one's emotional state or perception of personal appearance as well as distracting factors such as wires for data acquisition devices or instrumentation.

When comfort testing focuses on a device or product, it is important to consider the value proposition that the device provides the user. In some cases, the value of the device may influence the user's comfort threshold or thermal acceptability of the device.

COMFORT MODELS

Accurate assessment of thermal perception requires a comprehensive analysis of the heat transfer between the human body and the environment. A conventional prediction approach (e.g. PMV/PPD, Equivalent Temperature) is to directly correlate thermal perception to environmental conditions (e.g. air temperature, clothing), which implicitly accounts for the relationship between physiological state and thermal comfort [17][18][19]. An alternate approach (e.g. the Berkeley Comfort Model, Fiala DTS) is to explicitly correlate thermal perception to physiological state (e.g. skin and core temperature), thereby separating the objective thermal analysis portion of the problem from the subjective thermal perception analysis side [9][20][21][22][23].

Thus, thermal comfort models can be categorized as either environment-based [*Table 2*] or physiology-based [*Table 3*]. Environment-based models typically require inputs of air and surrounding temperatures, air velocity, clothing thermal resistances, humidity, and solar loading. Physiology-based comfort models just require inputs of the human body's thermal state, usually in terms of skin temperature, core temperature, evaporation rate, and the rates of change of skin and core temperatures.

Table 2: Examples of Environment-based Comfort Models	
Environment-based Models	**Publication**
Predicted Mean Vote (PMV)	Fanger 1970
Predicted Percent Dissatisfied (PPD)	Fanger 1982
Equivalent Temperature (EHT)	Wyon et al., 1989

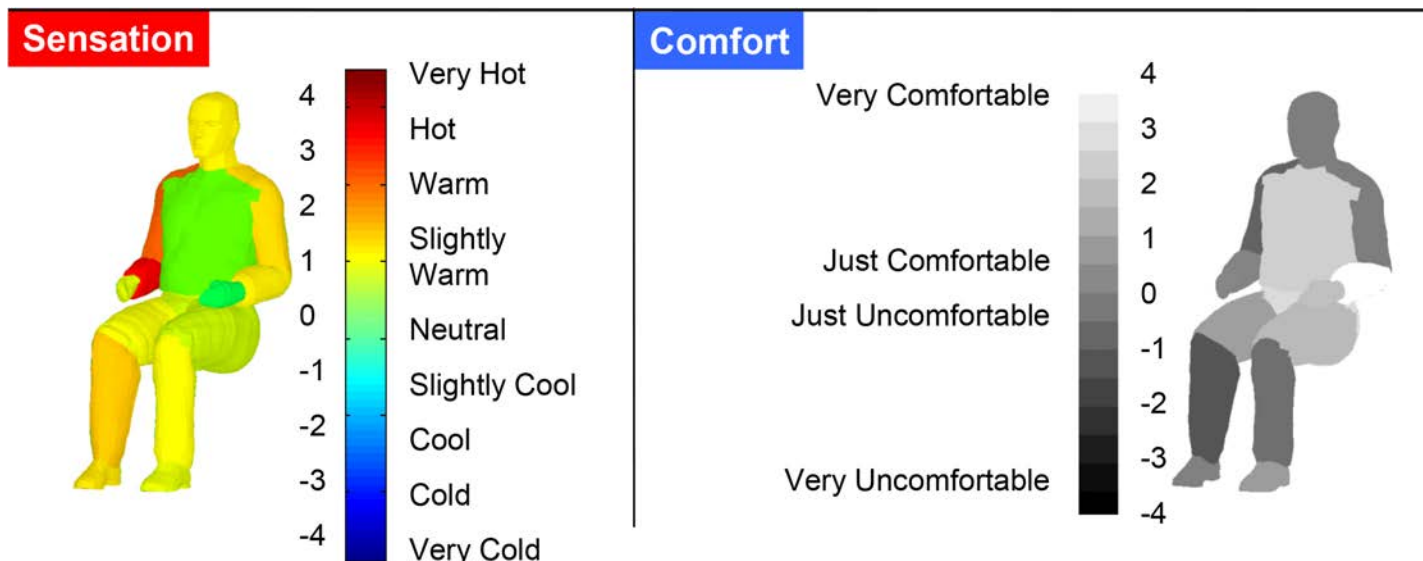| Table 3: Examples of Physiology-based Comfort Models	
Physiology-based Models	**Publication**
Skin Wettedness Comfort (w_{sk})	Gagge, 1967
Dynamic Thermal Sensation (DTS)	Fiala et al., 2003
Berkeley Comfort Model (BCM)	Zhang et al., 2009

Figure 3: Berkeley Comfort Model sensation and comfort

Fanger developed the Predicted Mean Vote (PMV) model and its associated Predicted Percentage of Dissatisfied (PPD) model to predict thermal sensation and the level of discomfort of human subjects in different steady environmental conditions and at various activity levels. Fanger's model is a function of activity level, clothing resistance, air temperature, mean radiant temperature, air velocity, and relative humidity.

Fiala's Dynamic Thermal Sensation (DTS) model is derived from correlations of thermal sensation with mean skin temperature, core temperature, and the time derivative of mean skin temperature. In contrast to PMV, the DTS model can be used to predict thermal sensation in transient conditions. Both PMV and DTS report thermal sensation on the ASHRAE seven-point scale in which +3 is hot, 0 is neutral and -3 is cold. The output from either model can be supplied to Fanger's PPD model to predict (dis)satisfaction with the thermal environment (i.e., thermal comfort), provided that conditions are both steady and homogeneous.

The Berkeley Comfort Model is widely considered the state of the art for predicting thermal perception from body core and skin temperatures in transient and asymmetric conditions. Overall and local (per segment) thermal sensation and comfort are reported on a pair of 9-point scales. The sensation scale has the same interpretation as the ASHRAE 7-point scale, but includes the extreme sensations of "very hot" and "very cold." A separate scale is used to indicate various levels of comfort; positive values indicating satisfaction and negative values corresponding to dissatisfaction.

Environment-based comfort models can be adequate for predicting comfort for individuals undertaking sedentary or low activity work for extended periods in traditional office building environments. Physiology-based comfort models, on the other hand, are needed to predict the comfort of individuals exposed to transient and asymmetric loading scenarios, or exposures in which an individual's anthropometry, physiology, or initial thermo-physiological state, play a role.

It is important to note that physiology-based comfort models must be used in conjunction with a high-resolution human thermal model that considers passive and active thermoregulation [24]. Metabolism, shivering, sweating, and changes in skin blood flow (vasomotion) must be modeled, often on a regional basis, so that human core and skin temperature distributions can be properly rendered before being input to a thermal comfort model.

INTEGRATION IN THE ELECTRONICS COOLING COMMUNITY

Physiology-based models are especially useful for predicting thermal perception within scenarios involving contact surfaces, such as a person occupying a heated and cooled seat, interacting with a consumer electronics device, or wearing clothing with passive or active heating and cooling technologies.

These models have found wide adoption in the automotive and architectural worlds. Many have been incorporated within standard heat transfer modeling tools. To better address the needs of the electronics cooling industry, the focus has recently shifted toward extending these models to accommodate comfort prediction for more localized heating effects. There are existing gaps and research areas that are actively being explored, such as the development of sub-segment models [*Figure 4*], accounting for ethnicity and psychology, and providing further physiologic and anthropometric resolution within the human body.
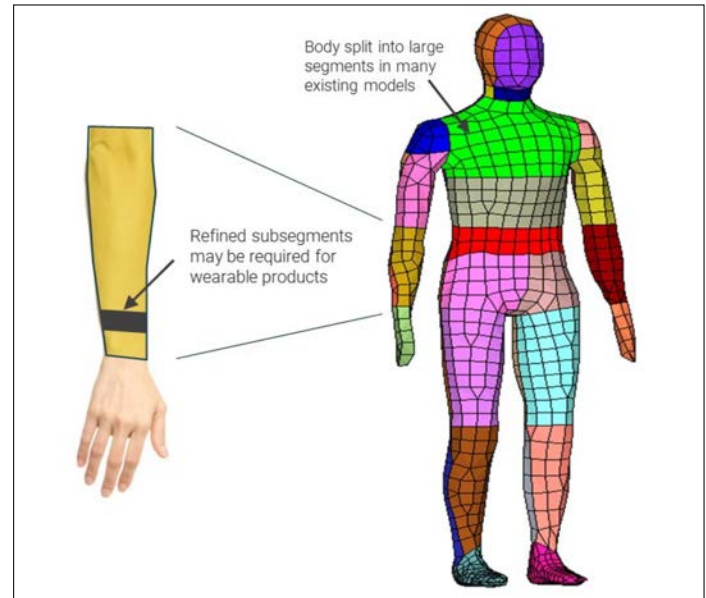

Figure 4: Sub-segment comfort zones

While a wearable electronic device may not significantly impact one's overall thermo-physiological state, it can significantly impact local thermal perception and lead to strong overall thermal comfort or discomfort, despite having limited contact with the body. Thermal discomfort surprises can be avoided through the integration of user comfort testing and physiology-based modeling into the standard design process for wearable electronics.

REFERENCES

[1] ASHRAE Standard 55, "Thermal environmental conditions for human occupancy," American Society of Heating, Refrigeration, and Air-Conditioning Engineers, 2010.

[2] IEC 62368-1, "Audio/video, information and communication technology equipment – Part 1: Safety requirements," International Electrotechnical Commission, 2018.

[3] Defrin R., Ohry A., Blumen N., and Urca G., "Sensory determinants of thermal pain," Brain, 2002.

[4] Griffith J., Hamilton A., et al., "Human skin temperature response to absorbed thermal power," Proc. SPIE 3037, Medical Imaging 1997.

[5] Ungar E., Stroud K., "A new approach to defining human touch temperature standards," 40th International Conference on Environmental Systems, 2010.

[6] ASHRAE Fundamentals, "Chapter 9: thermal comfort," American Society of Heating, Refrigeration, and Air-Conditioning Engineers, 2017.

[7] Fukazawa T., Havenith H., "Differences in comfort perception in relation to local and hwole-body skin wettedness," Journal of Applied Physiology, 2009.

[8] Ring J., de Dear R., "Temperature transients: a model for heat diffusion through the skin, thermoreceptor response and thermal sensation," Indoor Air. 1991;1:448–456.

[9] Gagge A.P., Stolwijk J.A., Hardy J.D., "Comfort and thermal sensations and associated physiological responses at various ambient temperatures." Environmental Research 1: 1 - 20. 1967.

[10] Schweiker M., Andre M., Al-Atrash F., Al-Khatri H., et al., "Evaluating assumptions of scales for subjective assessment of thermal environments – Do laypersons perceive them the way, we researchers believe?" Energy and Buildings, 211, 2020.

[11] Fanger, P.O., Melikov, A.K., Hanzawa, H., and Ring, J., "Turbulence and draft." ASHRAE Journal 31(4):18-25. 1989.

[12] Filingeri, D., Havenith, G., "Human skin wetness perception: psychophysical and neurophysiological bases," Temperature, 2:1, 86-104. 2015.

[13] Schweiker M., Huebner, G., Kingma, B., Kramer, R., and Pallubinsky, H., "Drivers of diversity in human thermal perception – A review for holistic comfort models," Temperature (Austin) 2018; 5(4): 308–342. 2018.

[14] Hepokoski, M., Curran, A., and Schwenn, T., "A Comparison of Physiology-Based Metrics to Environment-Based Metrics for Evaluating Thermal Comfort," SAE Technical Paper 2013-01-0844, 2013.

[15] ISO 14505-3:2006, "Ergonomics of the thermal environment — Evaluation of thermal environments in vehicles — Part 3: Evaluation of thermal comfort using human subjects," International Organization for Standardization, Geneva, 2006.

[16] Hepokoski, M., Patterson, S., Curran, A., Adelman, S. et al., "Evaluating a Heavy-Duty Truck Climate Control System Using Thermal Comfort-Focused Testing and Simulation Techniques," SAE Technical Paper 2019-01-0696, 2019.

[17] Fanger, P.O., "Thermal comfort analysis and applications in environmental engineering." McGraw-Hill, New York. 1970.

[18] Fanger, P.O., "Thermal comfort." Robert E. Krieger, Malabar, FL. 1982.

[19] Wyon, D. P., S. Larsson, et al., "Standard Procedures for Assessing Vehicle Climate with a Thermal Manikin." SAE Technical Paper Series 890049: 1-11. 1989.

[20] Zhang H., E. Arens, C. Huizenga, and T. Han, "Thermal sensation and comfort models for non-uniform and transient environments: Part I: Local sensation of individual body parts." Building and Environment, 2009.

[21] Zhang H., E. Arens, C. Huizenga, and T. Han. "Thermal sensation and comfort models for non-uniform and transient environments: Part II: Local comfort of individual body parts." Building and Environment, 2009.

[22] Zhang H., E. Arens, C. Huizenga, and T. Han. "Thermal sensation and comfort models for non-uniform and transient environments: Part III: Whole-body sensation and comfort." Building and Environment, 2009.

[23] Fiala, D., Lomas, K.J., Stohrer, M. "First Principles Modeling of Thermal Sensation Responses in Steady–State and Transient Conditions." ASHRAE Transactions, Volume 109, Part 1. 2003.
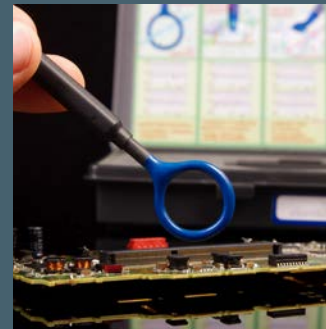
[24] Hepokoski, M., Gibbs, S. and Curran, A., "A new anatomical and thermophysiological description of a 50th percentile adult western male," Digital Human Modeling (DHM2016) Symposium, Montreal (2016).

EMCLIVE™

EMC LIVE 2022 is a series of **FREE**, online learning events designed for and by engineers in the EMC design and testing space. It features four separate one-day events, each focused on one of the most popular EMC areas in the industry:

Mil/Aero EMC | EMC Testing | Wireless/5G/IoT EMC | EMC Fundamentals

Attend an EMC LIVE event to learn the latest in EMC standards, equipment, theory, and design straight from the industry thought leaders.

Available Now

- **MIL/AERO EMC |** WATCH IT HERE ▶ https://emc.live/2022-event/mil-aero/

Coming Soon

- **TESTING EMC |** April 5, 2022
- **WIRELESS,5G & IOT EMC |** SEPTEMBER 20, 2022
- **EMC FUNDAMENTALS |** NOVEMBER 8, 2022

All for **FREE** | **WWW.EMC.LIVE**

Weibull Distribution

Ross Wilcoxon
Collins Aerospace

A little over a pandemic ago, the first article in this series on statistical analysis mentioned that a fundamental aspect of statistics is that one assumes a mathematical model that describes the distribution of a data set and then uses that model to estimate the probability that a given value or set of values will occur [1]. This allows us, for example, to estimate whether two sets of data are from the same underlying population or if they are statistically different. The statistical analyses discussed thus far have primarily assumed that a population has a normal distribution. However, there certainly are other distributions that can, and should, be used for different types of data. *Table 1* lists a few common statistical distributions with brief descriptions and examples of how they are applied.

Table 1 Common statistical distributions (adapted from Table 2.2 of Ref. [2])		
Distribution	**Field of Application**	**Example Applications**
Normal	Physical properties	Material properties, component values (such as resistance or capacitance), dimensions, etc.
Log Normal	Life phenomena of components; asymmetric distributions with large differences in observed values	Performance measurements for a population of systems such as cars, light bulbs, etc.
Weibull	Same as log normal and cases such as wear out, where failure rate changes	Life of components such as bearings, gears, electronic components, corroding materials, strength distribution of materials, survival probability in thermal cycling and shock, etc.
Exponential	System (multi-component) failures, including random failures	Non-wear out failures, life to failure of machines with many possible component failure modes
Binomial	Define correct sample size for assessing a large population with a known defect probability	Inspection for process / quality control. Sampled population large enough that parameters don't change when sampled
Hypergeometric	Same as Binomial, but for smaller populations	Probability of finding X defects out of a finite population of Y parts
Poisson	Situations where the number of occurrences can be measured, but not the number of times they don't occur	Long lines at the store, accidents, breakdowns, etc.

Lognormal and Weibull distributions are often applied to analyze reliability data for situations such as the wear out of solder joints that have been subjected to multiple thermal cycles. As a reminder, the formula for the probability of a given value of x in a normal distribution is shown in *Equation {1a}*. The mean, m, and standard deviation, s, for a population x can be easily calculated. Therefore, the probability distribution, f(x), of the normal distribution can be calculated directly with *Equation {1a}*. The cumulative distribution, F(x), which is the area under the probability distribution curve to the left of a value x, is found by integrating the probability distribution, as shown in *Equation {1b}*.

$$f_{normal}(x) = \frac{1}{\sigma\sqrt{2\pi}}exp\left[-\frac{(x-\mu)^2}{2\sigma^2}\right] \qquad \{1a\}$$

$$F(x) = \int_{-\infty}^{x} f(u)du \qquad \{1b\}$$

The lognormal distribution is also calculated using *Equations {1}*, except that the values of x that are used to calculate m, s, and f are all the natural logs of the population values.

The Weibull distribution is defined such that its cumulative distribution[1] is calculated as shown in *Equation {2}*.

$$F_{Weibull}(x) = 1 - exp\left[-\left(\frac{x}{\theta}\right)^\beta\right] \qquad \{2\}$$

As with the probability distribution of the normal distribution, the cumulative Weibull distribution can be directly calculated for any value of x once the two terms that characterize the distribution are known. Instead of the mean and standard deviation used in the normal distribution, the Weibull distribution uses the characteristic life (also known as the scale parameter), q, and the shape parameter, b. Physically, these two terms are similar to their normal distribution counterparts: the characteristic life is analogous to the mean, but instead of indicating the 50% failure point (for failure data), q corresponds to the point at which 63.2% (1-1/e) of the population would fail. Because of this, the characteristic life is often referred to as N63. The shape parameter, b, also known as the Weibull slope, is analogous to the inverse of the standard deviation. The larger the shape factor, the smaller the spread in the data.

While the Weibull coefficients (q and b) are physically analogous to the normal distribution coefficients (m and s), there are no formulas for directly calculating the Weibull terms as there are with the normal distribution terms. The Weibull coefficients can be calculated using a different approach that is ultimately at least part of the reason that the Weibull distribution has been widely used for analyzing reliability data.

The approach for determining the Weibull coefficients begins by first rearranging *Equation {2}*, as shown below.

$$\frac{1}{1-F(x)} = exp\left[\left(\frac{x}{\theta}\right)^\beta\right]$$

Taking the natural log of both sides of the equation twice gives us:

$$ln\left(ln\frac{1}{[1-F(x)]}\right) = \beta * ln\left[\frac{x}{\theta}\right]$$

This can be written as:

$$ln\left(ln\frac{1}{[1-F(x)]}\right) = \beta \ln(x) - \beta\ln(\theta)$$

This produces a linear equation of the form $Y = mX + C$, where the terms for Y, X, and C are:

$$Y = ln\left(ln\frac{1}{[1-F(x)]}\right), X = \ln(x), C = -m\ln(\theta)$$

Once the regression analysis has determined the linear coefficients m and C, they can be used to determine the Weibull coefficients. The shape factor is equal to the slope of the regression analysis (b = m) and the characteristic life is determined by rearranging the above equation for C as θ = exp(-C/m).

One easy way to generate a set of fatigue data is to count the number of times paper clips can be bent from 0° to 90°, as shown in *Figure 1*, before breaking. Data for the number of bends needed to break fourteen paper clips are shown in the first column of *Table 2*. As discussed later, this table also includes processed data used to calculate the Weibull coefficients. As shown in the bottom of the table, the measurements had an average of 17.5 bends with a standard deviation of 6.048.
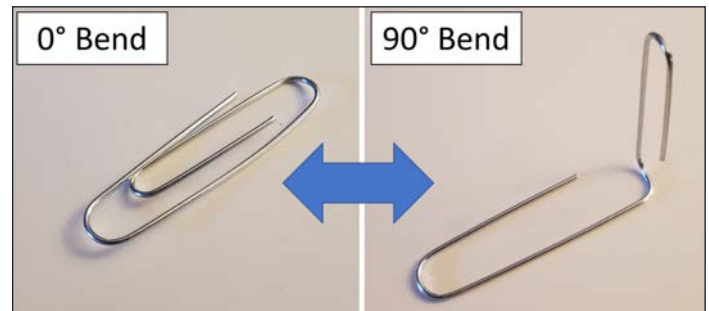

Figure 1 Paper clip fatigue test configurations

One possible way to define the cumulative failure distribution, F(x), would be to divide the rank of the failure by the total number of samples. For example, if 10 components are tested, the first failure would have F(x) = 0.1, the second one would be 0.2, etc. This approach, however 'pushes' F to higher values; for example, only the first failure would be categorized to the lowest 10% while the last two failures would be categorized to the highest 10%. A better approach for calculating the values of F(x) is to use the me-

---

[1] Interested readers can find the Weibull probability distribution function from any number of sources. Since it is somewhat less intuitive than the cumulative distribution and not really relevant to the point being made in this article, I'm not including it here.

dian ranks, which are typically calculated with *Equation {3}* [2]

$$F(x) = \frac{i - 0.3}{n + 0.4} \qquad \{3\}$$

In this equation, i is the rank of the failure and n is the total number of samples. For example, if 10 samples are tested, the first failure would have F(x) = (1-0.3)/(10+0.4) = 0.0673, the second failure would have F(x) = (2-0.3)/10.4 = 0.163, etc.

Since the calculation of F(x) requires that the order of failures be determined (first, second, etc.), the Excel @rank() function can be used to determine the order of failures[2]. Because of the way that this function deals with ties (each tie has the same rank), a small amount of 'noise' was added to the data to prevent any ties when calculating the ranks used for F(x). This noise was generated using the random function, which generates a random number between 0 and 1, by adding the term 'rand()/100' to the measured data, x, to create x*. The x* value was only used to determine the rank, which was then implemented in *Equation 3* to calculate F(x).

Table 2 Paper clip failures: raw and processed data				
Data	**Noise Added**		**Linearized Terms**	
x	x*	F(x*)	$ln\left[ln\left(\dfrac{1}{1-F}\right)\right]$	ln(x)
26	26.006	0.9514	1.107	3.258
14	14.007	0.3958	-0.685	2.639
15	15.005	0.4653	-0.468	2.708
22	22.009	0.6736	0.113	3.091
12	12.003	0.2569	-1.214	2.485
19	19.000	0.6042	-0.076	2.944
17	17.000	0.5347	-0.268	2.833
13	13.008	0.3264	-0.929	2.565
10	10.003	0.0486	-2.999	2.303
11	11.002	0.1181	-2.074	2.398
11	11.006	0.1875	-1.572	2.398
26	26.002	0.8819	0.759	3.258
24	24.000	0.7431	0.307	3.178
25	25.004	0.8125	3.219	0.515
17.5	<= average =>		2.806	
6.048	<= stan, dev. =>		0.351	

Once values of x and F(x) were determined, the linearized data of Y = ln(ln(1/(1-F) and X =ln(x) were calculated. Regression coefficients were determined using Excel functions m=slope(Y,X) and C=intercept(Y,X), as discussed in [3]. *Table 3* shows the values determined for m and C as well as the Weibull coefficients determined from them.

Table 3 Regression and resulting Weibull coefficients	
Regression slope, m	3.088
Regression intercept, C	-9.198
Shape Factor, β	**3.088**
Characteristic Life, θ	**19.66**

Notes
- *β = regression slope, m*
- *θ = exp(-C/m)*

Figure 2 plots the paper clip data along with corresponding fits of the data using many of the distributions listed in *Table 1*. The Excel equations used to generate these curves are shown in *Table 4*.
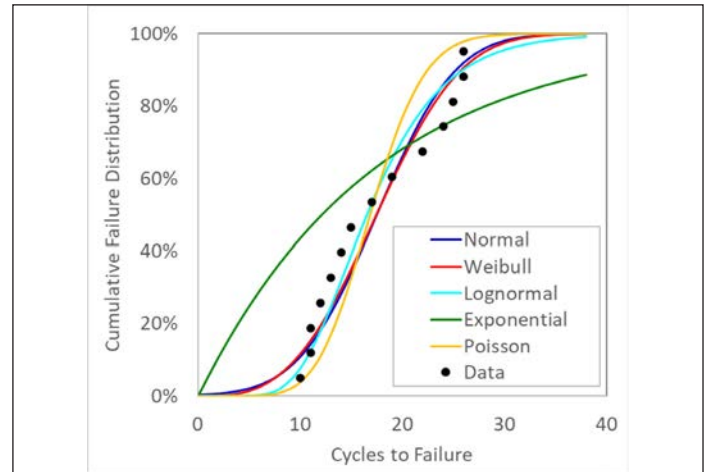

Figure 2 Paper clip data fit to different statistical distributions

Table 4 Excel functions used to calculate statistical distributions in Figure 2	
Distribution	**Excel Equation Used**
Normal	=NORM.DIST(N, 17.5, 6.048, TRUE)
Weibull	=1-EXP(-((N/19.66)^3.088))
Lognormal	=LOGNORM.DIST(N, 2.806, 0.351, TRUE)
Exponential	=EXPON.DIST(N, 1/17.5, TRUE)
Poisson	=POISSON.DIST(N, 17.5, TRUE)

Notes
- *Numerical values used in equations are shown in bold in Table 2 and Table 3.*
- *N is the number of cycles for which the CDF is found (for this plot, values of N = 2, 4, … 38 were used*
- *For Exponential distribution, a value of 24 gave a somewhat better fit than the population average*

An interesting observation from *Figure 2* is that, except for the Exponential distribution, all of the distributions provided a reasonably good fit to the measured data. The primary differences between the different distributions are in the tails and the knees (where F(x) ~0-10% and ~90-100%). One may then ask then, if the normal distribution, which is used almost everywhere, pro-

---

[2] The syntax to use this function to determine the rank of a value of X within a set of data Y, use =rank(X,Y,1) where 1 specifies ascending order so that the first failure is 1, the second failure 2, etc.

duces similar results to the Weibull distribution, why is Weibull primarily used for reliability analysis?

One reason is that Weibull distributions, as well as the other non-normal distributions shown, have a physically accurate limit. In those distributions, by definition, F(0) is equal to zero[3]. In contrast, a normal distribution of failure data includes some portion of the population supposedly failing at negative cycles. This is typically a small value - for the data in *Table 2*, the normal distribution calculates that 0.318% of the paper clips would fail before the first bend.

The much more important reason why the Weibull distribution has been used for assessing certain types of data, such as that from reliability testing, is that it does not rely on complete knowledge of the entire test population. If an entire set of samples is tested until all fail, the normal distribution – or better yet the lognormal distribution, which passes through F(0) = 0, will likely describe the data as well as the Weibull. However, due to constraints in time, budget, testing availability, etc., testing may stop before all samples have failed. If one characterizes the population only using that fraction of parts that have failed, the calculated average life will be much smaller since those components with longer lives would not be included in the calculations.

For example, if the paper clip testing had been stopped after a maximum of 15 bends, only half of the samples would have registered a failure. The average life of those parts would be 12.3 cycles, rather than the 17.5 that was found with the entire population.
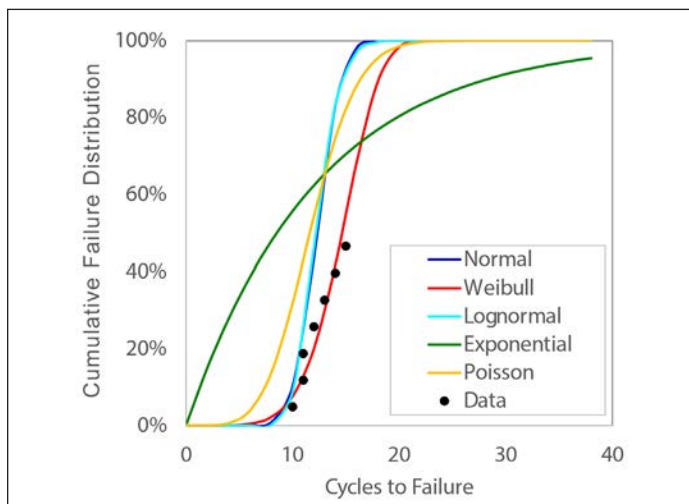
Figure 3 Failure distributions calculated only using failures up to 15 cycles

Figure 3 plots the same distributions as were shown in *Figure 2*, but with truncated data that only included those failures that occurred within 15 cycles. It is not surprising that those distributions that depend on the mean values, which were lower in the truncated

data, are pushed to the left and provide a less accurate description of the population of the entire data set. Because the Weibull distribution uses regression analysis of the failures as part of the entire test population, it continues to agree with the actual data.

Readers who are familiar with Weibull plots will notice that *Figure 2* and *Figure 3* use an unusual format for showing Weibull fits. Traditionally, those plots use linearized axes so that the data are shown relative to a straight line. *Figure 4* shows the data and the various distributions as plotted in this more conventional format.
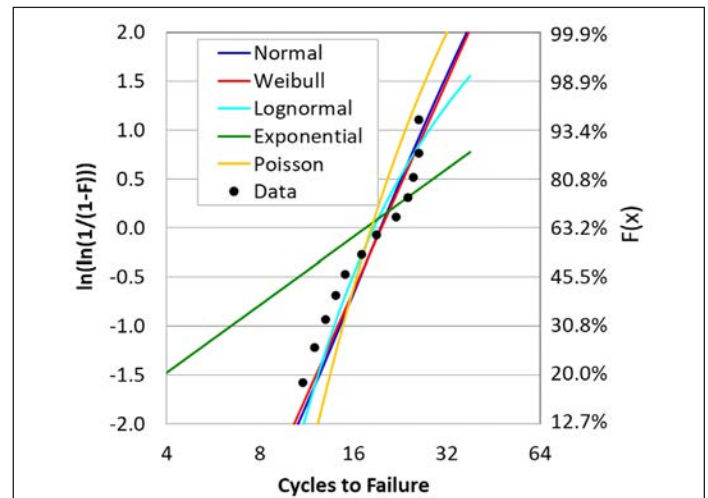

Figure 4 Paper clip data from Figure 2, plotted on linearized axes

CONCLUSIONS

This article briefly discussed statistical distributions other than the normal distribution and specifically focused on the Weibull distribution. The analysis presented here showed that most, but not all, of the distributions provided a reasonably good fit when data for the entire population were available. However, the Weibull distribution was also able to directly determine an accurate representation of reliability data, even when testing had been stopped before all samples were tested.

Different distribution models are used for different types of analyses. It is important that, when using these different distributions, one has some understanding of why a given distribution is typically used and to recognize its limits.

REFERENCES

1. Ross Wilcoxon, "Statistics Corner – Probability", *Electronics Cooling Magazine*, Spring 2020
2. J. S. Milton and Jesse Arnold, *Introduction to Probability and Statistics: Principles and Applications for Engineering and the Computing Sciences*, McGraw-Hill, 1986, pp. 297-308
3. Ross Wilcoxon, "Statistics Corner – Regression Analysis", *Electronics Cooling Magazine*, Fall 2021

---

[3] The 3-parameter Weibull distribution includes an additional value, x_0, which is offset value that forces the function to have a value of $F(x_0) = 0$. The term x_0, which corresponds to a failure-free life of the component, is physically useful but mathematically somewhat problematic since it prevents the Weibull distribution from being directly linearized.

2022 Company Products & Services Directory

In this section, we provide a quick guide to some of the top suppliers in each EMC category—in heat sinks, thermal testing, design services, and more. To find a product that meets your needs for applications, frequencies, standards requirements, etc., please search these individual supplier websites for the latest information and availability. If you have trouble finding a particular product or solution, email info@lectrixgroup.com for further supplier contacts.

	COMPANY	CONTACT INFORMATION	PRODUCTS & SERVICES	
MEDIA PROVIDER SPOTLIGHT	LECTRIX	LECTRIX 1000 Germantown Pike Plymouth Meeting, PA 19462 t: (484) 688-0300 w: www.lectrixgroup.com	– Strategy Firm – Full-Service Marketing – Publishing	– Events and Webinars – Custom Solutions – Training and Consultation
	electronics COOLING	Electronics Cooling 1000 Germantown Pike Plymouth Meeting, PA 19462 t: (484) 688-0300 w: www.electronics-cooling.com	– Media	– Training Seminars & Workshops
	thermalLIVE	ThermalLIVE™ Summit & ThermalLIVE™ 2022 | Online Events t: (484) 688-0300 e: info@electronics-cooling.com w: www.thermal.live	– Training Seminars & Workshops	

	COMPANY	WEBSITE	PRODUCTS & SERVICES	
A	Adaptive Corporation – A TriMech Company	www.adaptivecorp.com	– SIMULIA on 3DEXPERIENCE for Electromagnetic Simulation – CST Studio Suite for EMC/EMI	– Simulation and Thermal Design Services
	ALPHA	www.alphanovatech.com	– Coolers – Heat Sinks – Thermal Design Services	– Thermal Tapes – Thermal Testing
B	BOYD CORPORATION	www.boydcorp.com	– Blowers/Fan Accessories – Blowers – Chillers – Cold Plates – Fans – Gap Pads & Fillers	– Heat Pipes – Heat Sinks – Interface Materials – Liquid Cooling – Thermal Design Services – Thermal Testing
C	Cadence	www.cadence.com/en_US/home.html	– Software	
	CEJN USA	www.cejn.us	– Couplings	

	COMPANY	WEBSITE	PRODUCTS & SERVICES	
C	Celsia Inc.	www.celsiainc.com	– Heat Pipes – Heat Sinks – Heat Spreaders	– Thermal Design Services – Vapor Chambers
	CPC	www.cpcworldwide.com	– Connectors	
D	Delta Electronics (Americas) Ltd.	www.delta-fan.com	– Blowers – Fan Trays	– Fans – Heat Exchangers
E	Element Six Technologies	www.e6.com	–Chemical Vapour Deposition – Diamond Heat Spreaders	
	ELLSWORTH ADHESIVES	www.ellsworth.com	– Adhesives	– Encapsulants
F	Fujipoly® America Corp.	www.fujipoly.com	– Connectors – Gap Pads & Fillers	– Interface Materials – Thermal Design Services
	Future Facilities	www.futurefacilities.com	–Software	
H	Henkel	www.henkel.com	– Gap Pads & Fillers – Interface Materials – Phase Change Materials	– Substrates – Thermal Tapes
	Hexagon	www.hexagonmi.com/mscsoftware	– Software	– Training
I	Indium Corporation	www.indium.com	– Thermal Management Materials – Thermal Interface Materials	– Indium Metal
	Institution of MECHANICAL ENGINEERS	www.imeche.org	– Training Seminars & Workshops	
	ims	www.ims-resistors.com	– Heat Spreaders	– Thermal Management Devices
L	Laird Thermal Systems	www.lairdthermal.com	– Thermoelectric Coolers	- Liquid Cooling Systems
	LEADER TECH a HEICO company The Leading Edge In EMI/RFI Shielding Technology	www.leadertechinc.com	– Gap Pads and Filler – Interface Materialss	– Phase Change Materials

	COMPANY	WEBSITE	PRODUCTS & SERVICES
M	MALICO INC	www.malico.com	– Cold Plates – Heat Sinks	– Liquid Cooling
	MASTERBOND ADHESIVES | SEALANTS | COATINGS	www.masterbond.com	– Interface Materials
	Mersen	www.mersen.us	– Heat Pipes – Heat Sinks	– Liquid Cold Plates
N	Nanoramic Laboratories	www.nanoramic.com	– Interface Materials
P	Polymer Science Inc.	www.polymerscience.com	– Gap Fillers – Heat Spreaders	– Interface Materials – Phase Change Materials
R	Rosenberg USA, Inc.	www.rosenbergusa.com	– Blowers – Fan Filters	– Fans
S	Sager Electronics	www.sager.com	- Distributor of Electronics Components
	SCHLEGEL Electronics Materials	www.schlegelemi.com	- Thermal Interface Materials	- Gap Fillers
	SEMI-THERM	www.semi-therm.org	– Training Seminars & Workshops
	Shiu Li Technology Co., LTD	www.shiuli.com.tw	– Interface Materials	– Thermal Tapes
	SIEMENS	www.plm.automation.siemens.com/ global/en	– Software – Thermal Design Services	– Thermal Testing
	Staubli Corporation	www.staubli.com	– Connectors – Couplings	– Software

	COMPANY	WEBSITE	PRODUCTS & SERVICES
T	T-global Technology Co. Ltd	www.tglobal.com.tw	– Gap Pads & Fillers – Thermal Tapes – Interface Materials
	Thermal Engineering Associates Inc.	www.thermengr.net	– Thermal Test Chips
	TTI, Inc.	www.ttiinc.com	- Distributor of Electronics Components
U	Universal Sciences	www.universal-science.com	- Heatsinks - Interface materials - Peltier devices - Thermal substrates

Call for Authors and Contributors!

Want to be a part of the next issue of Electronics Cooling? Have an article or blog post you'd like to write for Electronics-Cooling.com?

Let us know at
editor@electronics-cooling.com

electronics COOLING

www.Electronics-Cooling.com

Index of
ADVERTISERS